University of South Carolina
Scholar Commons

2014

Classification of Low Velocity Impactors Using Spiral Sensing of Acousto-Ultrasonic Waves

Chijioke Agbasi
University of South Carolina - Columbia

Follow this and additional works at: https://scholarcommons.sc.edu/etd

 Part of the Mechanical Engineering Commons

Recommended Citation

CLASSIFICATION OF LOW VELOCITY IMPACTORS USING SPIRAL SENSING OF
ACOUSTO-ULTRASONIC WAVES

by

Chijioke Raphael Agbasi

Bachelor of Science
University of South Carolina, 2013

_____

Submitted in Partial Fulfillment of the Requirements

For the Degree of Master of Science in

Mechanical Engineering

College of Engineering and Computing

University of South Carolina

2014

Accepted by:

Sourav Banerjee, Director of Thesis

Victor Giurgiutiu, Reader

Joshua Tarbutton, Reader

Lacy Ford, Vice Provost and Dean of Graduate Studies

DEDICATION

I dedicate this work to my immediate family, most especially in loving memory of my late father, Engr. Ikenna Agbasi and brother, Tochukwu Ikenna Agbasi. My father's legacy as an engineer lives in me today, giving me the courage and confidence to continue in the discipline, and my brother's aspirations have become mine. I dedicate this work to my sweet mother, Maryrose Ikenna Agbasi, sisters, Ugochi Ikenna Agbasi and Chigozie Ikenna Agbasi, and brother Udochuckwu Ikenna Agbasi for their never ending support.

ABSTRACT

The non-linear elastodynamics of a flat plate subjected to low velocity foreign body impacts is studied, resembling the space debris impacts on space structures. The work is based on a central hypothesis that in addition to identifying the impact locations, the material properties of the foreign objects can also be classified using acousto-ultrasonic signals (AUS). Simultaneous localization of impact point and classification of impact object is quite challenging using existing state-of-the-art structural health monitoring (SHM) approaches. Available techniques seek to report the exact location of impact on the structure, however, the reported information is likely to have errors from nonlinearity and variability in the AUS signals due to materials, geometry, boundary conditions, wave dispersion, environmental conditions, sensor and hardware calibration etc. It is found that the frequency and speed of the guided wave generated in the plate can be quantized based on the impactor relationship with the plate (i.e. the wave speed and the impactor mechanical properties are coupled). In this work, in order to characterize the impact location and mechanical properties of imapctors, nonlinear transient phenomenon is empirically studied to decouple the understanding using the dominant frequency band (DFB) and Lag Index (LI) of the acousto-ultrasonic signals. Next the understanding was correlated with the elastic modulus of the impactor to predict transmitted force histories.

The proposed method presented in this thesis is especially applicable for SHM where sensors cannot be widely or randomly distributed. Thus a strategic organization

and localization of the sensors is achieved by implementing the geometric configuration of Theodorous Spiral Sensor Cluster (TSSC). The performance of TSSC in characterizing the impactor types are compared with other conventional sensor clusters (e.g. square, circular, random etc.) and it is shown that the TSSC is advantageous over conventional localized sensor clusters. It was found that the TSSC provides unbiased sensor voting that boosts sensitivity towards classification of impact events. To prove the concept, a coupled field (multiphysics) finite element model (CFFEM) is developed and a series of experiments were performed. The dominant frequency band (DBF) along with a Lag Index (LI) feature extraction technique was found to be suitable for classifying the impactors. Results show that TSSC with DBF features increase the sensitivity of impactor elastic modulus, if the covariance of the AUS from the TSSC and other conventional sensor clusters are compared. It is observe that for the impact velocity, geometric and mechanical properties studied herein, longitudinal and flexural waves are excited, and there are quantifiable differences in the Lamb wave signatures excited for different impactor materials. It is found that such differences are distinguishable only by the proposed TSSC, but not by other state-of-the-art sensor configurations used in SHM. This study will be useful for modeling an inverse problem needed for classifying impactor materials and the subsequent reconstruction of force histories via neural network or artificial intelligence.

Finally an alternative novel approach is proposed to describe the Probability Map of Impact (PMOI) over the entire structure. PMOI could serve as a read-out tool for simultaneously identifying the impact location and the type of the impactor that has impacted the structure. PMOI is intended to provide high risk areas of the space

structures where the incipient damage could exist (e.g. area with PMOI > 95%) after an

impact.

TABLE OF CONTENTS

LIST OF FIGURES

x

xi

LIST OF ABBREVIATIONS

AHM .... Active Health Monitoring

ANN .... Artificial Neural Network

AU .... Acousto-ultrasonic

AUS .... Acousto-ultrasonic Signal

CFFEA .... Couple Field Finite Element Analysis

CFFEM .... Couple Field Finite Element Method or Model

CFFES .... Couple Field Finite Element Simulation

CZ .... Clerence Zener

DFB .... Dominant Frequency Band

FEM .... Finite Element Method

FET .... Feature Extraction Technique

GW .... Guided Wave

HME .... Health Monitoring Event

LI .... Lag Index

PHM .... Passive Health Monitoring

PMOI .... Probability Map of Impact

POI .... Probability of Impact

PZT .... Lead Zirconate Titanate

SHM .... Structural Health Monitoring

SOV .... Space Operating Vehicle

STFT .... Short Time Fourier Transform

CHAPTER 1

INTRODUCTION

Structural Health Monitoring

The vast sub-field of non-destructive evaluation (NDE), so called structural health monitoring SHM, has evolved tremendously. SHM is broadly referred to as the development and implementation of a damage identification strategy for aerospace, civil, and mechanical engineering infrastructure [1]. SHM can be dated back to the early 19th century when rail wheel inspectors used the acoustic emission from a harmer strike upon a wheel for damage detection [2]. Today, SHM involves advanced sensing such as in the application of AU smart structures. In the early years of NDE, a similar sub-field known as non-destructive testing (NDT) was more proliferated. Techniques like Thermoelastic Stress Analysis (TSA) also referred to as SPATE (Stress Pattern Analysis by Thermal Emission) were found useful for the direct measurement of stress and insipient damage via thermoelastic correlation [3]. The time required to perform SPATE tests and its repeatability were found undesirable [4, 5] and efforts were made to improve the technology such as Sapphire-L1and FAST. Although these efforts were successful, in general, the technique required considerable human operation; thereby, making it not suitable for next generation online health monitoring systems.

For the past two decades, a considerable amount of work has been done towards the advancement of SHM systems in order to detect and manage unhealthy events such impact loads, propagating cracks and corrosion promptly, which has led to the safer and

more reliable operation of engineering infrastructures [6-8]. In recent years, the concept of SHM has evolved to meet the ever growing demands of our technology-driven world. SHM platforms are now designed to be automatic and implement time saving artificial neural network (ANN) that are linked, in most advanced cases wirelessly, to in situ sensing platforms. ANN SHM systems are based on the blue print of the biological nervous system. Intelligence is enabled by the harmonious network of passive sensors (an analogy to our sensory neurons) that receive physical signals, and active sensors (an analogy to the biological motor neurons) that excite signals. For an elucidation of the deliberate analogy-driven design of ANN from the nervous system see [9-12]. The advantage of ANN is its fast processing capabilities. SHM systems operating ANN are installed on host structures for simultaneous passive and active sensing, and execute probability density functions or simply "voting" towards the classification of health monitoring events (HMEs). Depending on the enabled functionalities, SHM platforms can interrogate the host structure to detect, diagnose, and classify unhealthy events through appropriate data processing tools and designed algorithms capable of performing robust non-linear function approximation [13]. By ANN SHM systems, condition based maintenance (CBM) is possible, because instead of periodic maintenance that is heavily expensive and inefficient, maintenance is carried out according to system requirement. State of the art SHM platforms can be trained to automatically classify online events in host structure with a certain level of confidence, making maintenance demand driving and guarantying positive economic impacts [9, 14].

Sensitivity and reliability of SHM platforms is paramount since it involves life-safety. An unbiased voting system of sensors constituting the forefront of the ANN is

crucial for correct classification of HMEs. Consequently, a tremendous amount of research work has been done to develop robust SHM technology, which has lead to a variety of sensing techniques available for a variety of damage identification scenarios. Hassan et al [15] applied a nonlinear vibration interaction metric for assessing the health conditions of AH-64 helicopter tail rotor drive shafts in effort to manage nonlinearities in data. The metric was based on a cross-bispectrum analysis, which is the Fourier transform of the second order correlation function. Molina used AU technique combined with pattern recognition for the characterization of polymeric material degradation when subjected to repeated impact [16]. Giurgiutiu et al [9, 17] extensively studied the use of piezoelectric wafer active sensors (PWAS) for active health monitoring (AHM). AHM is enabled transceiver function (i.e. pitch-catch technique). Embedded PWAS probe the structure as well as listen for excited signals. Insipient damages such as crack and corrosion have been identified and classified from the transmitted or reflected signals using this technique. Yang et al [27] through AHM developed an attenuation based model that used signal energy and specific damping capacity as selected features for the classification of loose fasteners in SOV thermal protection panels. In this thesis work, a robust and structured platform capable of investigating and classifying low velocity, low energy impact events on structures through its inherent mutually exclusive voting capabilities is studied. This type of work is particularly useful in the aerospace industry where flight vehicles are vulnerable to dynamic impacts from small random objects.

Simultaneous identification of impact locations and impact objects is challenging in the field of SHM and almost absent. This work aims to use the AU waves excited during a low velocity, low energy impact to identify the probable impact location and classify

3

the impactor elastic modulus. By classifying the impactor elastic modulus, highly sensitive prediction of insipient damage can be further determined although not reported in this work. Prominent damage prediction techniques used in the industry include Ultrasonic C-scan, radiography (x-ray/gamma ray), optical microscopy, scanning electron microscopy (SEM), scanning acoustic microscopy (SAM), and Digital Image Processing (DIC), only to name a few [18-20]. It can be observed that these techniques are not suitable for next generation SHM because they require heavy hardware and mobility over the host structure in order to function in real time. In addition, they require considerable human intervention. This means that a PHM system that is light weight, on board, automated and can accurately predict insipient damages arising from low velocity, low energy impacts is highly sought after in today's SHM.

This thesis work proposes a physics-based feature extraction approach and presents two techniques for this referred to as the dominant frequency band (DFB) and lag index (LI) that classify the impactor material property. In addition, an alternative approach referred to as the Probability Map of Impact (PMOI) is also presented. Such techniques are implemented on a novel sensor configuration cluster called the Theodorus Spiral Sensor Cluster (TSSC) that is capable of enhanced sensitivity. "Theodorus Spiral" (TS) is the orientation of the PZTs used for this novel approach. The sensors are clustered at a particular position on the structure following the pattern. This proposed sensor configuration facilitates strategic placement of the discrete sensors in the cluster, enabling the acquisition of mutually exclusive signals. Performance of TSSC in characterizing the impactor types is compared with two conventional sensor configurations. Focus is given to the vigilance function of the sensor configuration. This vigilance function is aka

4

passive health monitoring (PHM); however, studies can be further extended to AHM. In fact passive and active health monitoring are both necessary for a complete smart structure, since the former accounts for impact classification while the latter accounts for damage prognosis. For PHM, it is discovered that the Theodorus Spiral is a powerful geometry for casting the probability map of impact (PMOI) that discerns the impact location and impact type. It is envisaged that when an impact event occurs, TSSC installed on the host structure in proximity to impact will begin to acquire mutually exclusive acoustic signals, and then transmit the acquired data to a black-box containing a combined physics and statistical data-driven processor that will classify the impact event accordingly.

1.1 IMPACTOR TYPE AND FORCE HISTORY IDENTIFICATION FOR STRUCTURE HEALTH MONITORING

The non-linear elastodynamics of a flat plate due to a low velocity, low energy non-uniform foreign body impact is studied experimentally in this work. The study is performed in order to characterize the impactor type and consequently predict the impact force history. The motivation is based on a central hypothesis that in addition to identifying the impact locations, the material properties of the foreign objects can be classified using transmitted AUSs, for a more accurate damage prediction. Boundary conditions of the plate, the geometry and the mechanical properties of the impactors and the plate, the impact velocity, etc. influence the nature of transmitted energy in the plate in form of GWs. Transient displacements, contact area and transmitted stresses are unknowns and the physical event is simultaneously influenced by the impact and plate's response [21]. This study reveals that there is a quantifiable difference in the Lamb wave

signature excited for different impactor materials. Frequency and consequently speed of the GWs generated in the structure can be quantized based on the impactor relationship with the structure, i.e. the wave speed and the impactor mechanical properties are coupled. The quantization is achieved through the features extracted from the AUSs, which are then combined with theoretical results for an automated and a more accurate solution approach. Dominant frequency band and Lag Index are the physics-based features utilized in this thesis work. They provide an unconventional way to investigate and relate the impactor-plate dynamics. Such investigations with their highest resolution are quantified as a result of the proposed Theodorus spiral configuration of the sensors (TSSC). Findings are applicable to next generation passive health monitoring systems that implement wired or wireless ANN that smartly sense impact events by classifying the impactor type/material. Such a function is completely absent in current state-of-the-art SHM methods. SHM should include smart sensing capability that classifies the impact type (e.g. Teflon-like or Steel-like impactor material, or small or large contact area impact). This provides smart structures with the ability to better predict the degree of damage. For an enhanced sensitivity, acoustic emissions from impact events are obtained via mutually exclusive discrete sensors. On this note, a comparative study is done amidst the sensor clusters that can be directly applied to simple neural networking platforms for online SHM as easy read out tools. We focus our study on low velocity, low energy impacts in the range specified in Figure 1.1. These impact events are more probable to cause insipient damages and are the more difficult to classify. Damage will depend on impact parameters such as velocity of impact, size, material property, and consequently,

effective energy of impact. Our objective is to classify these parameters using sensible features in the excited AUS through the boosted GW sensitivity of the TSSC.
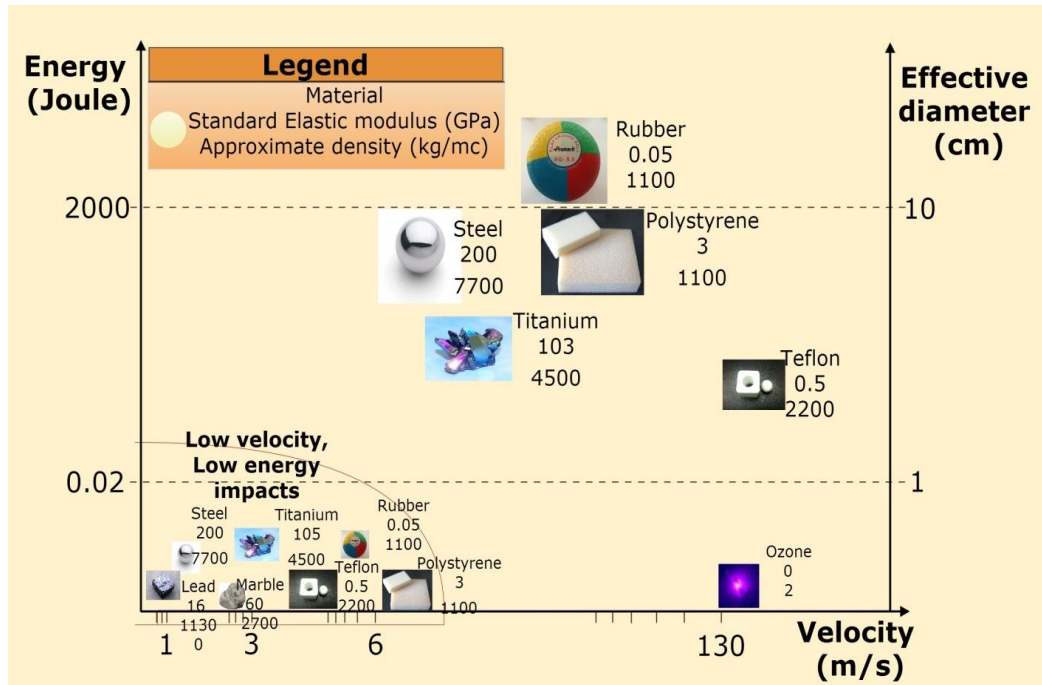
Figure 1.1 Impactor types according to velocity, density, energy, size, and elastic modulus

1.2 PROBABILITY MAP OF IMPACT (PMOI) FOR STRUCTURE HEALTH MONITORING

Exterior components of SOVs are susceptible to impact events from debris present in the outer-space or debris aerodynamically sheared off from the structure itself due to aerodynamic heating. Similarly, aircrafts are susceptible to impacts from maintenance tools and flying birds during maintenance and operating conditions, respectively. Modern, lightweight speed-trains are also susceptible to impacts from foreign objects laying on the train-tracks. Approximate estimation of impact location and impact type (i.e. the impactor mechanical and geometric property as well as impact energy and force

history) in passive mode facilitates SHM systems to predict damage or suggest further investigation of the impact region using the active mode for more accurate damage information. To replicate such impact events for scientific studies, generally the physical event is idealized as a flat plate and a spherical solid impactor in the laboratories. This approach is adhered to in this thesis work.

An alternate technique called the Probability Map of Impact (PMOI) for locating the impact region and classifying the impact type is presented in this work and it is implemented on the TSSC as well. This technique discretizes the impacted structure into small pixels and for each pixel computes a representative PMOI value instead of a final impact location value. The PMOI approach eliminates the need for a selecting a wave velocity when determining the impact location. The contour map of the Probability of Impact (POI) demonstrates the most probable location of impact. In addition, its geometric parameters with respect to certain threshold values reveal further information on the impact type. Fundamental to this study is the guided wave (GW) aka Lamb wave propagation that can be sensed by piezoelectric sensors as AUSs. Once PMOI is obtained from the proposed approach, the region on the structure having a POI > x% can be further investigated with the same set of sensors in active mode. Here the x% is the threshold value of the POI and can be problem dependent or importance dependent (e.g. > 95% or 98%).

1.3 RELATED WORKS

Most plate impact analyses separate the impact event into a local contact problem at the impact location and a global problem for the plate response. However, this does not

capture the true phenomena. Conventionally, the Hertzian contact law is implemented for the analysis of the local response from which the contact force can be theoretical derived. Yang J and Chun [22], Sun and Yang S [23], Suemasu et al [24], Liu and Swaddiwudhipong [25], Olsson [26], Zheng and Binienda [27] all employed the Hertzian contact law in their formulations. Clerence Zener (1941) proposed an analytical solution for an isotropic plate impacted by a spherical impactor using infinite Hertzian and Kirchhoff-Love theory [28]. Olsson (2000) showed that small mass and large mass impactors of identical impact energy initiate different plate response [29]. Lee et al [21, 30, 31] studied the transmission of energy flow in plate from a structural intensity approach. In this thesis work, a simultaneous study on the influence of the impactor mechanical properties on the transmitted force history and plate elastodynamics is conducted, both empirically and numerically, and an alternative approach referred to as the PMOI is proposed for both impact localization and impact classification.

Among many applications using GWs, detection of impacts and resulting defects in plate-like structures have received great attention [32-35]. Generally, a network of piezoelectric (PZT) transducers is exploited to develop a real time SHM system using active-passive mode [36] or passive mode [37]. In traditional active-passive mode, some PZTs act as an acoustic source and some act as receivers/sensors. The wave signals received by the receivers are analyzed to find the time of flight (TOF) and through a technique known as the Triangulation technique the damage location can be estimated. However, this approach has been found to possess a fundamental barrier to accurately locating the damage since it depends on selecting the appropriate velocity from the velocity profile of the structure, [38] which is affected by several other factors such as the

frequency of the guided wave, homogeneity of the wave guide, impact type, environmental conditions, etc. The velocity dependence of the triangulation technique makes the technique prone to error unlike the proposed PMOI which is not dependent on wave velocity. In passive mode, sensors are used for monitoring impacts from foreign objects which act as acoustic sources [39, 40]. In reality, the time of the impact and location are unknown but the event can be captured by the receivers operating in passive mode. Modern technology permits sensors to begin data recording when the acoustic energy crosses a certain threshold in one of the sensors. This function is usually referred to as the 'trigger' function. Trigger information can be sent to all sensors in the network and the acoustic event can be recorded by multiple sensors for a stipulated period of time. This is a fundamental approach in SHM and it is known as the Acoustic Emission (AE) technique [41]. The strategies for locating the acoustic source can be divided into three major techniques discussed subsequently [38].

Direct strategies allow the location of the wave source to be detected by capturing the wave direction of propagation without the prior knowledge of TOF. This method requires anisotropic transducers that are capable of detecting the direction of the incoming waves. Matt et al. [42], Salamone et al [43] proposed an approach based on transducer rosettes comprised of Macro-Fiber Composite (MFC) transducers. Salas et al. [44] proposed the use of composite long-ranged variable-direction emitting radar (CLoVER) transducer for excitation of the guided wave.

Inverse optimization methods have been developed for impact force history and damage identification in composite and stiffened structures. An inverse method based on system identification technique by using the transfer function was proposed by Park et al.

[45]. Staszewaski et al [46, 47] proposed a procedure for impact detection using neural network and genetic algorithm approaches, although in some cases these models become unstable, and from a computational or data storage point of view, such procedures require an extensive number of training observations prior to deployment, making them quite onerous [48]. However, physics-based FE reduces the number of training needed.

Hyperbolic positioning algorithms locate the impact by using the arrival time difference of the wave fronts captured by sparse array of sensors. Usually, most of the methods for developing this algorithm utilize the triangulation technique (also known as Tobias Algorithm), wherein the impact point is identified as the intersection of three circles, whose centers are the sensor location. This approach is strongly limited by the assumption that wave velocity must be known and remains the same in all directions, which is rarely the case especially for the anisotropic and inhomogeneous materials. Also, soft impactors generally excite flexural wave modes in the structure. This becomes a problem because the wave velocity of the flexural wave modes are not constant but are a function of frequency which in turn depends on the rate of indentation and amount of energy transmitted into the plate. Due to the dispersive nature of the impact event, a suitable choice of time-frequency analysis for the identification of TOF is necessary.

Kundu et al [49] proposed a method based on optimizing an objective function by using the threshold-based procedure to find the time differences. However, the proposed objective function in that reference had the inherent problem of multiple singularities which was overcome in [50] by modifying the objective function. The optimization technique was further improved by Hajzargerbashi et al [51]. Other procedures for detecting the time differences are peak detection techniques [52, 53] or

cross-correlation technique [54]. However, the precision of these methods is limited by dispersion and noisy acquisition, which complicate the exact time of arrival detection. In [55] and [56], the nonlinear least square optimization adopting the Gauss-Newton method was proposed to determine the location, time lag, and velocity of the 'synthetic' AE signal. Ciampa and Meo [57] used Newton's iterative method to calculate the co-ordinates of the impact location and wave velocity.

For AUS data acquisition in this work, AE technique is implemented. The acquired AUSs are passed through the aforementioned physics-based FETs, which are the DFB and LI. In addition to this, the AUSs are also passed through a time difference computation and objective error function optimization algorithm that computes the PMOI. Although conventional triangulation technique works well for the isotropic plate by processing the AUSs (generated by the impact phenomenon) acquired by at least three sensors, the technique assumes that the impact point is inside a triangle made by the three sensors, which makes it inherently suitable for distributed sensor network. If the plate is anisotropic, this method does not work well. On the other hand, optimization technique, which is based on a minimization of a non-linear objective function or error function, works well for anisotropic plate and has been demonstrated by earlier researchers [49, 50], although for this technique to work well in anisotropic structure, the direction dependence of the wave velocity must be known, which might not be feasible for large structures. On this note, a velocity independent method is considered and achieved by clustering 3 sensors at close proximity, such that the variation of wave velocity sensed by the sensors remains close to each other and within close error bounds. Errors can be significant as a result of insufficient number of voting sensors. The all new TSSC concept

is proposed to solve this problem by using spirally oriented PZTs, which are efficiently utilize for the voting process. To the best of the authors' knowledge, none of the passive techniques presented in the literature take advantage of this special orientation of the PZTs. A sub-cluster of multiple combinations of three sensors with variable arm length instigates the concept of spiral pattern of sensors and TSSC for impact point identification and impactor classification. TSSC is placed in proximity such that distant impact event can be monitored with increased reliability and wave velocity independence.

Considering the impact points are sufficiently far away from the TS (location is at least greater than the largest arm of the TS), it can be assumed that the wave velocity does not change significantly. This feature of the spiral will be very helpful for impact point identification in both isotropic and anisotropic plates. The inherent characteristic of TS is that it has varying radius and angles, making its orientation sensitive to different wave numbers. Another important feature of the proposed spiral pattern is that along every direction there are at least three sensors with varying distance. This feature provides both the direction and frequency sensitivity, which improves the impact type characterization techniques. TSSC is employed for many particular and practical reasons that are discussed in the next chapter.

CHAPTER 2

SENSOR CLUSTER SELECTION

There are many geometric configurations to choose from when designing a sensor cluster, for example a line, square, circle, triangle, any chiral geometry or spirals e.g. Theodorus spiral, Archimedean spiral, logarithmic spiral, golden spiral, 3-angle spirangle, 7-angle spirangle, etc. However, there are some attributes of geometries that make them ideal for specific applications. In SHM, linear, square, circular, and star sensor clusters have been well studied and can be recursively found in literatures [9, 58-60]. These geometries are useful for phased array beamforming and object detection, generally because of their uniformity and ease of reference. Similarly, in undersea vessel detection as well as microphone array technology, circular sensor arrays combined with cylindrical architecture are preferably used because of their acoustic impedance adjustability, immunity to left-right uncertainty inherent in linear arrays, and 360° beamforming capabilities [61, 62]. Rarely the spiral geometries are used in NDE applications. Known to the author, only one work exist so far in literature that applies spiral sensing technology to SHM [34]. AHM work by Byungseok et al. [63] applied a steered directivity function and differential array response to data obtained from a cluster of spiral arrays which determined the location of damage on a plate. To the best of author's knowledge no application of spiral sensing is reported for PHM.

However, besides SHM applications, spiral mathematics is being used in many other applications. Few examples include the logarithmic spirals of the class log-aesthetic

curves (LACs) that have been used in computer aided design for the generation of visually pleasing curves and aesthetic surfaces (e.g. car bodies) [64]. In the field of image processing, spiral architecture has been applied to data registering in place of rectangular grid in order to combat the inefficiency of processing pixels in rows and columns. This means that instead of registering images in a hard-coded two coordinate system, addresses can be operated using spiral algebra that operate independently from the actual coordinates [65]. Improvement in angular resolution is made possible by hexagonal pixels of spiral architecture inspired by the primate's striate cortex [66-68]. It is no surprise that nature utilizes spiral geometry for efficient data processing of the physical world. The cochlea in the human ear is another instance where spiral architecture exists; however, the purpose of this thesis is not to exhaustively enumerate the applications of spirals but present the usefulness of TSSC for SHM. Apparently, spirals have been found very useful. The TS makes it easy to control the distribution of sensors in a clustered layout while obtaining 100% mutually exclusive data sets. This feature will be useful for ANN because all sensors will simultaneously contribute distinctly towards impact event localization and classification. TS theory and TSSC are discussed next.

2.1 THEODORUS SPIRAL (TS) THEORY

TS geometry starts with a right angle triangle at the origin O and propagates in a spiral network of contiguous right angled triangles that are constrained by the origin and its unit projected normals. Figure 2.1 (a) shows the projected normals from the origin and how the angles between two vertices of the spiral with respect to the origin vary. The angles can be simply obtained as

$$\theta_n = \sum_{k=1}^{n-1} arctan\left(\frac{1}{\sqrt{k}}\right), \quad n = 0,1,2,\dots \qquad (2.1)$$

and the change in angle as

$$\theta_{n+1} - \theta_n = arctan\left(\frac{1}{\sqrt{n}}\right). \qquad (2.2)$$

The equal length constraint for the triangles' external lines is specific to TS exhibiting the "construction of Anderhib" [69]. Anderhib postulated this constraint to explain why Theodorus stopped his discussion of the spiral at $\sqrt{17}$. Anderhib observed that the resulting snaillike figure constructed with this constraint was a range of right angled triangles that were non-overlapping.

The parametric form of the TS was derived by PJ Davis (69). Davis began his derivation with the understanding that the location of the vertices z_n of the spiral can be mathematically modeled in the complex plane, iteratively, by the equation

$$z_{n+1} = z_n + i\frac{z_n}{|z_n|}, \qquad i = \sqrt{-1}, \qquad (2.3)$$

where $z_0 = 1$, for example. Having knowledge from the hypotenuse values of the contiguous triangles, $|z_n| = \sqrt{n+1}$ and equation (2.3) can be rewriting as

$$z_{n+1} = \left(1 + \frac{i}{\sqrt{n+1}}\right)z_n. \qquad (2.4)$$

Equation (2.4) is a linear, homogeneous difference equation with non-constant coefficients. It computes what is called the *discrete spiral of Theodorus*. With this equation, the layout of the TS can be simply obtained. However, inspired by Euler's infinite product for the *gamma function*, Davis revised his equation (2.4) to better represent the spiral. The revised equation was given as
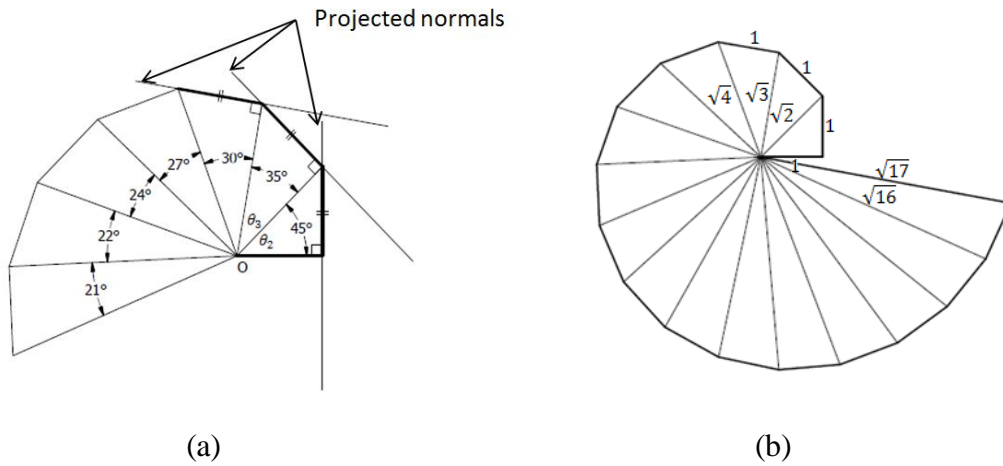
Figure 2.1 Constructing TS. (a) Projected tangents and changing angle θ (b) The spiral of Theodorus displaying the "construction of Anderhub"
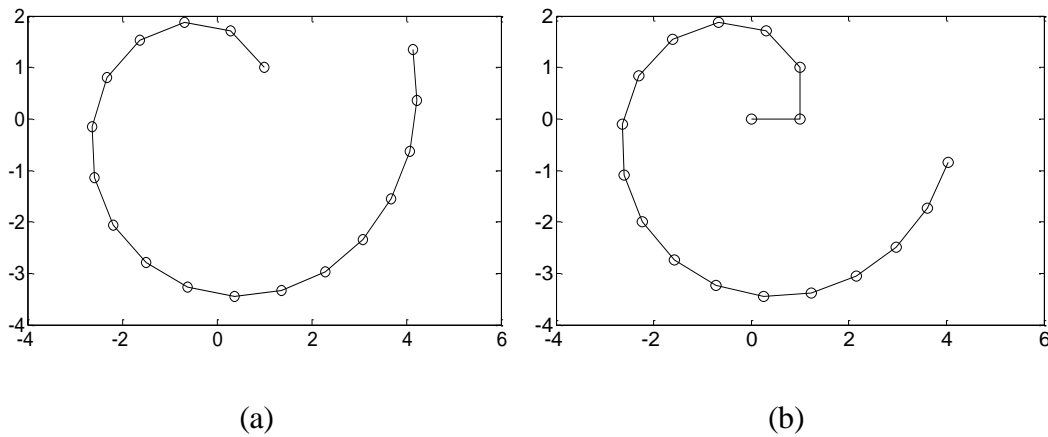
Figure 2.2 Equation based construction of TS (a) using equation (2.4) (b) using equation (2.5)

$$T(e) = \prod_{k=1}^{\infty} \frac{1 + \frac{i}{\sqrt{k}}}{1 + \frac{i}{\sqrt{k+e-1}}}, \qquad e > -1. \qquad (2.5)$$

where e is the nth vertices of the spiral or what will become the nth sensor of the TSSC.

This function is called the *Theodorus function* in honor of Theodorus [69]. The function

maps the vertices of the spiral towards the origin as e decreases from ∞ to 0 and away

from the origin as e increases. Figure 2.2 compares TS obtained using both equations (2.4) and (2.5). It can be seen that equation (2.5) better satisfies the "construction of Anderhib" than equation (2.4).

2.2 JUSTIFICATION OF TSSC

The importance of TS geometry for SHM is in the distinct location of its vertices. No two vertices are symmetric in any way or overlap because vertex location is determined by the angle function θ_n given in equation (2.1) and radius function $T(e)$ given in equation (2.5). As shown in Figure 2.3 (a) the projected dash-lines along each hypotenuse side of the right-angled triangles in TS do not overlap, confirming distinctness of vertex positions. These vertices are useful for strategic "discrete sensor" placement in the design of ANN sensor clusters. Signals obtained from such a sensor cluster layout are mutually exclusive, thereby assuring efficient use of the discrete sensors in the cluster as well as robust characterization of HMEs. Although mutually exclusive signals can also be acquired by random placement of sensors, TS facilitates an organized and clustered layout which in term make wiring and connection of the sensors to hardware less cumbersome for practical application. This organized cluster feature is very helpful for critical areas of the structure where sensor broad distribution may not be feasible or broad wiring is a hassle. TSSC is also applicable to beamforming techniques that use pitch catch and differential array to detect damage, although not explored in this thesis work. One additional importance of TS for SHM is its inherent ability to enhance wave mode and frequency sensitivity because of its varied arm lengths.

When comparing TS to conventional sensor cluster geometries like circle or square, it is easy to observe that (Figure 2.3 (b)) inherent symmetry exists among the

18

discrete sensors in circle or square cluster with respect to an incident wavefront. This is the same case for other linear sensor arrays. Opposite mode vectors would have symmetric components such as

$$k_1 sin\theta = k_2 cos\theta \qquad (2.6)$$

$$k_1 cos\theta = k_2 sin\theta \qquad (2.7)$$

where k_1 and k_2 are wave vectors passing through the centers of the top left and right sensors. k_n is considered as the nth mode vector that passes through the center-line with respect to the cluster. All the other mode vectors are taking to pass through a center of a discrete sensor. The mode vectors displayed in Figure 2.3 (b) pass through the center of colored sensors. TS has no mode vectors observing equations (2.6) and (2.7); hence no symmetry exists in sensing mode. For wave vector k_n, a circle and square cluster will have three sensors collinear with this wave vector; thereby, making two of the three sensors redundant. However, TSSC has only one sensor collinear with the wave vector. TSSC overcomes the situation of redundancy and inefficiency because all its discrete sensor positions are non-symmetric and unbiased. Equation (2.6) and (2.7) show how two symmetric mode vectors in a CSC or SSC can be decomposed into their orthogonal components to confirm them mere images of one another. This means that symmetric sensors will be unable to capture mutually exclusive data sets. In a CSC and SSC, more than half the sensors in the cluster acquire biased information about HMEs, thereby making them inefficient for ANN. Inefficiency in acquiring mutually exclusive signals may not be an issue in AHM where beamforming, pulse-echoes are implemented for damage inspection. However, in PHM signals from an acoustic emission such as an arbitrary impact event could travel in a variety of unknown modes and could mix with

19

noise or other impact events. It becomes necessary to implement a device that can sense a range of wave modes in order to detect unhealthy ones. Consequently, this makes the solution cheaper, because some of the hardware channels that are dedicated in circle and square cluster platforms are found to be useless or redundant. However, TSSC makes all sensors valuable. In the next chapter, we shall discuss plate waves for an understanding of the type of wave modes that propagate in plates and are sensed by the discrete sensors.

(a)   (b)
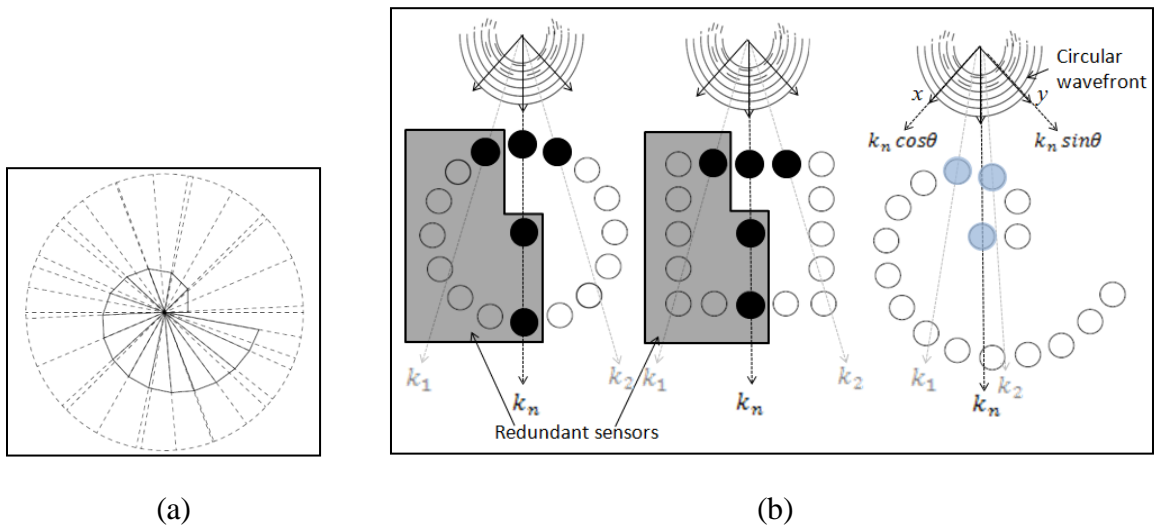
Figure 2.3 The distinctness in the vertices of TS. (a) Projected non-overlapping hypotenuse lines. (b) Redundancy due to symmetry and in-line sensors of a circle and square sensor cluster compared with non-symmetry and non-overlapping hypotenuse network of TS.

CHAPTER 3

PLATE IMPACT

In this chapter the theory of plate response to non-uniform impact is discussed. First of all, the general physics of plate waves is discussed, and following, is the analysis of the unique problem of plate elastodynamic response due to impactor-plate coupled mechanical properties, from which modifications to an existing theory is proposed.

3.1 PLATE WAVE THEORY

Plate waves aka Lamb waves or guided waves transport energy within the boundaries of plate-like media. These waves can be excited by impact or by a transducer in contact with the plate. The theory of Lamb wave propagation was first described by Horace Lamb (1917) and then further elucidated by Viktorov (1967). It has been used extensively for understanding the elastodynamics of plate-like structures (e.g. space shuttle panels) and for the development of a broad range of SHM techniques. Shear horizontal (SH) wave is another plate wave, but not usually exploited because of its difficulty to be experimentally measured due to its in-plane particle motion and also because it is negligible in SHM. Lamb waves on the other hand are typically useful since they transmit most of the ultrasonic energy. Lamb waves are easily detectable using conventional sensors. Lamb waves are highly dispersive in nature. They are of two categories, symmetric and antisymmetric, of which both have multiple modes. The symmetric modes (S0, S1, S2, . . .) exhibits symmetric displacement and stress along the

21

mid-plane of the plate. Similarly, the antisymmetric modes (A0, A1, A2, . . .) exhibits antisymmetric displacement and stress along the mid-plane [9]. As the values of frequency thickness product (fd) increases, higher order symmetric and antisymmetric modes appear. As the fd value decreases, after a cut off fd value the mode number reduces to the fundamental modes, A0 and S0. With further proximity to a zero fd product, the fundamental modes further reduce to plate axial wave aka extensional or longitudinal wave and flexural wave aka deformational wave. Plate axial and flexural wave speeds are given by,

for axial wave speed, c_L

$$c_L = \sqrt{\frac{E}{(1 - \sigma^2)\rho h}}, \qquad (3.1)$$

and for flexural wave speed, c_F

$$c_F = \left(\frac{G}{\rho h}\right)^{\frac{1}{4}} \sqrt{\omega}, \quad G = \frac{Eh^3}{12(1 - \sigma)}, \qquad (3.2)$$

where E is the elastic modulus, σ is the Poisson ratio, ρ is density, h is the plate thickness, G is flexural stiffness, and ω is the wave frequency. Knowing the plate properties, we can calculate the theoretical wave speeds. We shall see later in the paper that the excited acoustics waves from the low energy impacts studied herein are the fundamental modes that can be adequately approximated by the axial and flexural waves.

Lamb waves and shear horizontal waves originate from the particle motion wave equation of the general partial differential form

$$-\mu \nabla^2 \mathbf{u} - (\lambda + \mu) \nabla (\nabla \cdot u) = \rho \ddot{\mathbf{u}}, \qquad (3.3)$$

where $\mathbf{u}$ is the particle displacement vector, λ and μ are the Lame parameters, and ρ is the density. The solution of the wave equation (3.3) is solved by assuming appropriate

wave potentials and imposing the surface stress free boundary conditions. The resulting equations have non-trivial solutions when the determinant of the coefficient matrix is taking to be equal to zero. A detailed derivation can be sought in [9, 70]. For brevity, only the Lamb wave equations are discussed further.

Symmetric modes take the form

$$\frac{\tan pd}{\tan qd} = -\frac{(\xi^2 - q^2)^2}{4\xi^2 pq} \qquad (3.4)$$

and Antisymmetric modes take the form

$$\frac{\tan pd}{\tan qd} = -\frac{4\xi^2 pq}{(\xi - q^2)^2} \qquad (3.5)$$

where $p^2 = \frac{\omega^2}{C_p^2} - \xi^2$, $q^2 = \frac{\omega^2}{C_s^2} - \xi^2$. C_p^2 is the pressure wave speed also called the longitudinal, dialational, compressional, axial, or primary wave (P-wave) speed of a 3-D solid media. Similarly, C_s^2 is the shear wave speed aka distortional, transverse, secondary wave (S-wave) speed of a 3-D solid media. ξ is the mode number, d is the half thickness of the plate. The Lamb wave modes are plotted in Figure 3.1 for a 1mm thin aluminum 2024-T3. This plate will be used later in our models. Superimposed on the plots are the plate axial and flexural wave speeds. Noticeable at low frequencies of about 500 kHz is that the S0 mode can be approximated by the plate's longitudinal wave. Applying equation (3.1), it is found that longitudinal wave speed or phase velocity for the aluminum plate in this region is typically around 5400 m/s. In addition, below a frequency of about 80 kHz and speed of 1000 m/s the A0 mode can be approximated by the plate's flexural wave.
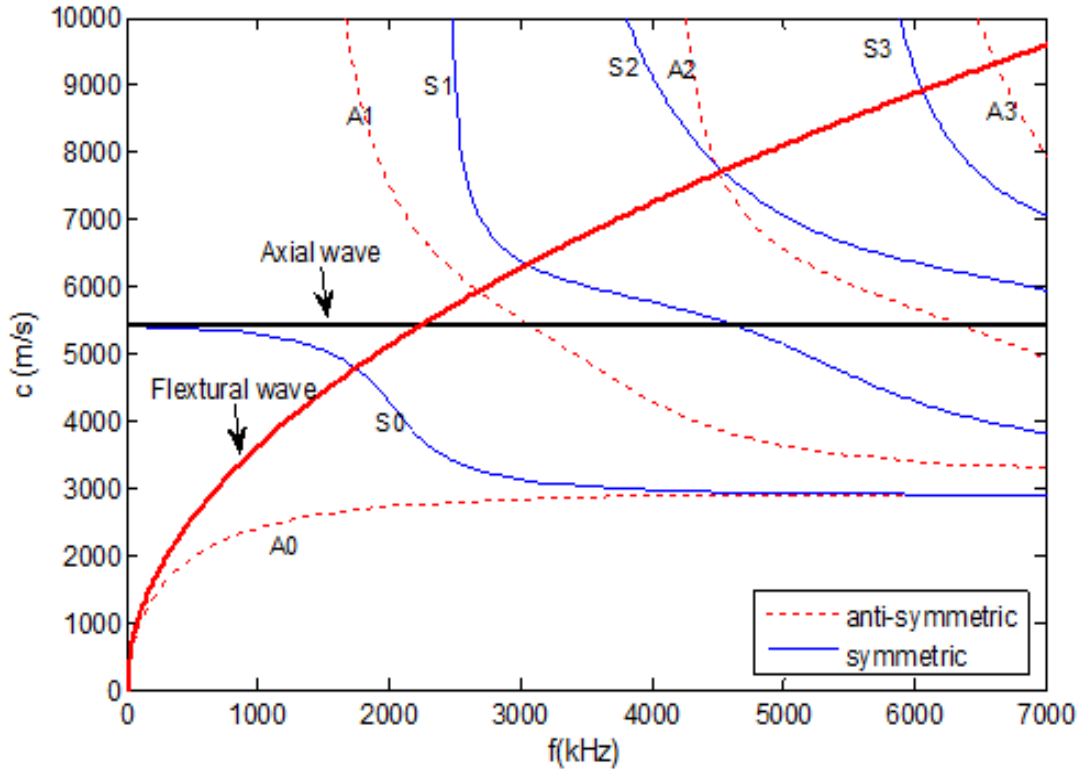
Figure 3.1 Lamb wave phase velocity of Aluminum-2024-T3

3.2 TRANSMITTED FORCE DUE TO NON-UNIFORM IMPACT

For a small displacement in a flat plate, we use the unified particle motion equation given by

$$\mu\nabla^2\mathbf{u} + (\lambda + \mu)\nabla(\nabla \cdot \mathbf{u}) + \mathbf{f} = \rho_p\ddot{\mathbf{u}} + \mathbf{F}, \qquad (3.6)$$

where, $\mathbf{u}$ is the particle displacement vector, λ and μ are the Lame parameters, ρ_p is the density of the plate, $\mathbf{f}$ is the body force, and $\mathbf{F}$ is the externally transmitted force [9, 70]. The homogenous solution of the equation (3.6) (i.e. $\mathbf{F} = \mathbf{f} = 0$) yields the solution of shear horizontal wave and coupled Lamb waves as discussed in the previously in the previous section. However, in impact analysis it is important to note that the externally applied load $\mathbf{F}$ is not zero. It is non-uniform and is transmitted with a natural intensity

24

factor e that is governed by the unique coupled properties of the impactor and plate given by

$$\mathbf{F} = \ddot{u} \, e(E_{p,i}, \rho_{p,i}, \sigma_{p,i}, w, R) \int_c \rho_p \, dxdydz, \quad (3.7)$$

where, $E_{p,i}$ is the elastic modulus of the plate p and the impactor i, likewise ρ is the density, σ is the Poisson ratio, w is the plate thickness and R is the radius of the impactor. The objective is twofold:

(1) Accurately estimate the material properties of the impactors.

(2) Experimentally investigate $\mathbf{F}$ and correlate with the TSSC sensor signals.

Although previous work has been done to derive the closed form solution of the plate local and global response due to impact load [28, 71], the uniqueness of the solution of Lamb waves excited by random impactors on plate is indetermininistic. Therefore, we use the signature of the signal at a distance d from the impact after degeneration of the particle displacements due to damped wave propagation and geometric spreading of energy to predict the probable impact force profile. The received AUSs degenerate according to the following equation, where b is the function of coupled material properties.

$$\ddot{u}_{\mathbf{d}} = \frac{1}{\sqrt{d}} e^{-bd} \ddot{u}. \quad (3.8)$$

For hard material spherical impactors on the plate, the displacement and force history at the point of impact can be analytically approximated by Clarence Zener's (CZ) theory; however, for soft material impactors like Teflon, there are huge discrepancies. Consequently, data driven indices are constructed for more accurate results. Accurate results are needed for damage prediction, which will depend on the force transmitted or

dissipated in the structure particularly due to the coupled plate-impactor properties. CZ theory accords with the fact that force history of the impact event is dependent on coupled physical properties of the impactor and the plate, from which a dimensionless parameter λ is determined. In this analysis, we shall express all parameters in their respective domain except otherwise stated, keeping the plate parameters constant in order to isolate impactor parameters. CZ theory is applicable to the impact events whose impulse acted are concluded before the arrival of the reflected waves from the plate boundaries. It is safe to assume that the impact events are elastic and complete after the impactor to plate collision, pressure exertion and retraction. However, the displacement on the plate at the point of impact remains perfectly inelastic until the boundary reflections return to the origin [28]. The first equation is the acceleration of the impactor modeled as a spherical body and is given by

$$m \frac{d^2 s}{dt^2} = -F, \qquad (3.9)$$

where s is taken as the displacement of the center of the sphere in contact with the plate, m is its mass, F is the plate reaction. Displacement of the mid-plane of the plate at the point of impact is said to be directly proportional to impulse and is expressed as

$$Z = \left(\frac{3\rho_p}{E_p'}\right)^{0.5} \frac{P}{16\rho_p w^2}, \qquad E' = \frac{E}{1 - \mu^2}, \qquad (3.10)$$

$$Z = \alpha \int F dt, \qquad (3.11)$$

where Z is the point on the mid-plane of the plate underneath the impact point, P is impulse, and α is a constant of proportionality determined from Kirchhoff-Love theory by imposing fixed boundary and initial conditions of a square plate. It is then sought to

express the plate reaction as a function of the relative displacement U between the center of the sphere and the mid-plane of the plate in the form

$$U = s - Z. \qquad (3.12)$$

Equation (3.12) is differentiated twice [28] and subtracted from equation (3.9) to obtain the governing equation of motion of the plate impact event given by

$$m\frac{d^2 U}{dt^2} + \alpha\frac{dF(U)}{dt} + F(U) = 0, \qquad \text{given at } t = 0 \begin{cases} U = 0 \\ \dfrac{dU}{dt} = v_0 \end{cases} \qquad (3.13)$$

where v_0 is the initial velocity of the impactor. The governing equation (3.13) is a nonlinear ordinary differential equation. The interaction of plate and sphere is nonlinear and is approximated explicitly by classical Hertzian contact theory for a half-spaced impacted solid:

$$F(U) = kU^{1.5} \qquad (3.14)$$

$$k = \left(\frac{4}{3}\right)r^{\frac{1}{2}}\left(\frac{E_p' E_i'}{E_p' + E_i'}\right). \qquad (3.15)$$

Here, k is the contact stiffness that depends on the elastic parameters E_p' and E_i' of the plate and impactor respectively, which in turn depends on Young's modulus E and Poisson ratio μ. As mentioned in [27], equation (3.14) can be modified to account for finite thickness of the plate by rewriting as

$$F(U) = \varsigma kU^\varepsilon \qquad (3.16)$$

where ς is a constant that accounts contact force reduction in the plates due to finite thickness and the exponent ε takes the limits $1 < \varepsilon < 3/2$. Substituting equation (3.14) into (3.15) and then into (3.13), the resulting equation can be integrated numerically to obtain the contact force history of the impact event at the point of impact. Force history plots can be obtained for any impactor and plate dynamic contact. For all force history plots in

27

this work, the plate properties were kept constant and the impact energy H is approximated by

$$H = mgh = \frac{1}{2}mv_0^2. \qquad (3.17)$$

H is also kept constant, as well as the effective diameter of the impactor (i.e. the diameter of the sphere) in order to simplify the problem and study only impactor material effects. As a result, solutions obtained were a function of the mechanical properties of the impactor. Here, g is acceleration due to gravity and h is the drop height of the sphere which was varied to equalize the impact energy and nullify the energy effect.

3.3 MODIFIED CLERENCE ZENER THEORY

After conducting several experiments in the laboratory of idealized impact events on a plate, it was found that the theory developed by Clerence Zener is not sufficient to accurately capture the transient force profiles particular to the soft impactors, especially in the time domain. Transient characteristics of the force profiles due to the impacts are important to understand the nonlinear plate response and further necessary for predicting the damage occurrence more accurately, because of the effect of wave-controlled impact [27] or energy dissipation as opposed to plastic shear and deformation [72]. Short duration impacts have compact force profiles that transmit through-thickness waves dominated by longitudinal waves aka P-wave and found to be a characteristic of the hard material impactors. On the other hand, long duration impacts are dominated by shear and flexural waves aka S-wave that is found to be a characteristic of the soft material impactors. Consequently, we propose two feature extraction techniques, experimentally and numerically determined, to be capable of characterizing impactor elastic modulus

28

from the plate waves. From this information, impactor type can be identified and subsequently, the transmitted force history can be accurately estimated. Although previous authors have proposed iterating ς or ε defined in equation (3.16) in order to provide more accurate results, it is observed that these parameters only influence the force peaks and do not reconstruct the transient profile of the transmitted force accurately. One this note, two new parameters: β and γ are introduced in the non-dimensional equation formulation in order to control and account for numerical contact time discrepancy and viscoeleastic dissipation, respectively. To introduce these two new parameters we make the transformation as follows.

$$\sigma = \frac{s}{v_0 T}; \qquad \tau = t \left(\frac{\beta k v_0^{0.5}}{m} \right)^{-0.4}, \qquad (3.18)$$

$$\lambda = \frac{\pi^{0.6}}{3^{0.5}} \left(\frac{r}{2w} \right)^2 \left(\frac{\rho_i}{\rho_p} \right)^{0.6} \left(\frac{v_0}{v'} \right)^{0.2} \left(\frac{E_i'}{E_p' + E_i'} \right)^{0.4}, \qquad (3.19)$$

where v' is velocity defined by

$$v' = \left(\frac{E_p'}{\rho_p} \right)^{0.5}. \qquad (3.20)$$

Hence, the motion equation (3.13) can be modified to account for contact time discrepancy and viscoeleastic dissipation according to

$$\frac{d^2\sigma}{d\tau^2} + (\lambda + \gamma) \frac{d\sigma^{1.5}}{d\tau} + \sigma^{1.5} = 0, \qquad \text{given at } \tau = 0 \begin{cases} \sigma = 0 \\ \frac{d\sigma}{d\tau} = 1 \end{cases} \qquad (3.21)$$

CHAPTER 4

MODELING A MONITORED IMPACT EVENT

Recently, coupled field finite element analysis (CFFEA) has become a cost effective and reliable approach for advanced science and engineering analysis. Various academic, governmental and industrial disciplines employ this method because it provides the freedom of combining various physics in a single model for performing complicated simulations. For this same reason, we employ CFFEA to efficiently simulate and study impact events as an addition to empirical results. A CFFEM is developed for the efficient evaluation of the three sensor cluster configurations previously displayed in Figure 2.3 (b). Sensor electric potentials are obtained from the modeled sensor clusters that undergo piezoelectric effects.

4.1 COUPLED FIELD FINITE ELEMENT MODEL OF A SIMPLIFIED IMPACT EVENT

The CFFEA is carried out in ABAQUS-Dynamic Implicit. ABAQUS-Dynamic Implicit was desired for its ability to simulate the combined non-linear impact event and piezoelectric transduction inherent in this work. ABAQUS-Dynamic Implicit employs a Hilber-Hughes-Taylor time integration scheme, which is unconditionally stable when the α-dissipative parameter is in the limits: $-\frac{1}{2} \leq \alpha \leq 0$ [43]. The Hilber-Hughes-Taylor time integration scheme is an advancement over the Newmark Beta method, allowing

adjustability of dissipative properties without affecting solution accuracy of the lower

modes [73].

Table 4.1 Material properties of employed specimens (the values reported are standard specifications that were optimized by experiments and finite element simulations).

Material	E. Modulus (GPa)	Density (Kg/m^3)	Poisson's ratio
Stainless Steel	200	7750	0.29
Titanium	103	4521	0.37
Aluminum 2024-T3	72	2780	0.33
Marble	30	2685	0.23
Polytetrafluoroethylene (PTFE) aka Teflon	0.5	2214	0.46

Abaqus-Dynamic Implicit provides continuum elements in conjunction with

piezoelectric elements. The CFFEA package fully supports the complexity of the physical

event studied herein. Simulations of controlled impact events are performed to test the

feature extraction technique and TSSC proposed in this work. All simulations consisted

of the following components: an isotropic plate, an impactor simplified as a spherical

body, and a cluster of seventeen piezoelectric sensors. The isotropic plate was made of

(305x305x1) mm thin Aluminum 2024-T3 and its boundaries were fixed. 17 piezoelectric

sensors were embedded on the plate in three interchangeable configurations. The three

31

configurations were a circle sensor cluster (CSC), a square sensor cluster (SSC), and TSSC. Then the plate was impacted. For each sensor configuration, the plate was impacted with four different impactors; made of stainless steel, titanium, marble and Teflon (see Table 4.1 for material properties), respectively. These materials were chosen to represent hard, intermediate, and soft materials. The impact energies were equalized by varying their impact velocities calibrated by their mass according to equation (3.17).

10-noded quadratic tetrahedron elements (C3D10) were used to discretize the impactor, 8-noded linear quadrilateral in-plane general-purpose continuum shell elements (SC8R) were used to discretize the isotropic plate, and lastly 8-noded linear piezoelectric elements (C3D8E) where used to discretize the piezoelectric sensors. The sensors were modeled as disc-shaped APC-850 Lead Zirconate Titanate (PZT) sensors with the following reasonable material properties

$$P_{pe} = \begin{bmatrix} 0 & 0 & 0 & 0 & 10.2 & 0 \\ 0 & 0 & 0 & 10.2 & 0 & 0 \\ -7.4 & -7.4 & 20.5 & 0 & 0 & 0 \end{bmatrix} \frac{\text{C}}{\text{m}^2} \quad (4.1)$$

$$K_{pe} = \begin{bmatrix} 86 & 37 & 37 & 0 & 0 & 0 \\ 37 & 86 & 37 & 0 & 0 & 0 \\ 37 & 37 & 77 & 0 & 0 & 0 \\ 0 & 0 & 0 & 23 & 0 & 0 \\ 0 & 0 & 0 & 0 & 20 & 0 \\ 0 & 0 & 0 & 0 & 0 & 20 \end{bmatrix} \text{GPa} \quad (4.2)$$

$$D_{pe} = \begin{bmatrix} 951 & 0 & 0 \\ 0 & 599 & 0 \\ 0 & 0 & 951 \end{bmatrix} \times 10^{-8} \frac{\text{F}}{\text{m}}. \quad (4.3)$$

Here, P_{pe} is the piezoelectric matrix, K_{pe} is the stiffness matrix and D_{pe} is the dielectric matrix. Density was stipulated as 7700 kg/m3, diameter was 8.75mm, and thickness was 0.560mm. The piezoelectric sensors were bonded to the surface of the plate using a tie function in ABAQUS. The tie function enables surface to surface bonding and quick

mesh transition, thereby making meshing less intensive (see Figure 4.1 (e)) [74].

Piezoelectric effect or piezoelectric permittivity pe produces a polarized vector in the thickness direction when an internal stress is induced in the piezoelectric structure by the propagating elastic waves on the plate. The P_{pe} matrix linearly operates on the stress vector, producing electrical displacements also called electrical potentials. With these assignments, the non-linear to linear transient elastodynamics of a spherical impactor striking a plate is simulated, and consequently, the profile of the generated lamb waves via the in situ piezoelectric structures undergoing electrical excitations is obtained.

Critical element size was determined by the contact area made by the impactor on the plate. This was the critical region of the model. Selective meshing was applied to the whole model with the impact region being the densest. A common rule of thumb for element size is 25% of the smallest wavelength of the propagating wave. This premise was applied to the coarsest regions of the model. The impact region was the finest region of the model as seen in Figure 4.1 (b) and (c). Based on a convergence studies performed to design the CFFEM, the critical element size was determined to be about 20% of the contact diameter. This was also confirmed to be sufficient by performing a rough estimation of the indentation-η caused during the virtual impact. This was can be estimated using the Hertzian solution of a spherical body in contact with a plane, given by

$$\eta = \frac{(3\pi)^{\frac{2}{3}}}{2} P(e_1 + e_2)^{\frac{2}{3}} \left(\frac{1}{D}\right)^{\frac{1}{3}}, \quad e_{1,2} = \left(\frac{1 - \sigma_{1,2}}{\pi E_{1,2}}\right), \quad (4.4)$$

where, η is the indentation depth, P is the total load applied which in this case is the peak dynamic load expected from the impact event, D is the diameter, $\sigma_{1,2}$ are the Poisson

ratios of the sphere and plane respectively, likewise $E_{1,2}$ are the elastic moduli [75]. By applying simple geometric analysis upon η, the contact diameter and area can be computed. It was found that for the spherical impactor which was 5 mm in diameter, the resulting contact diameter is about 1.6E-2 mm; hence a critical element size of 3E-3 mm would suffice.
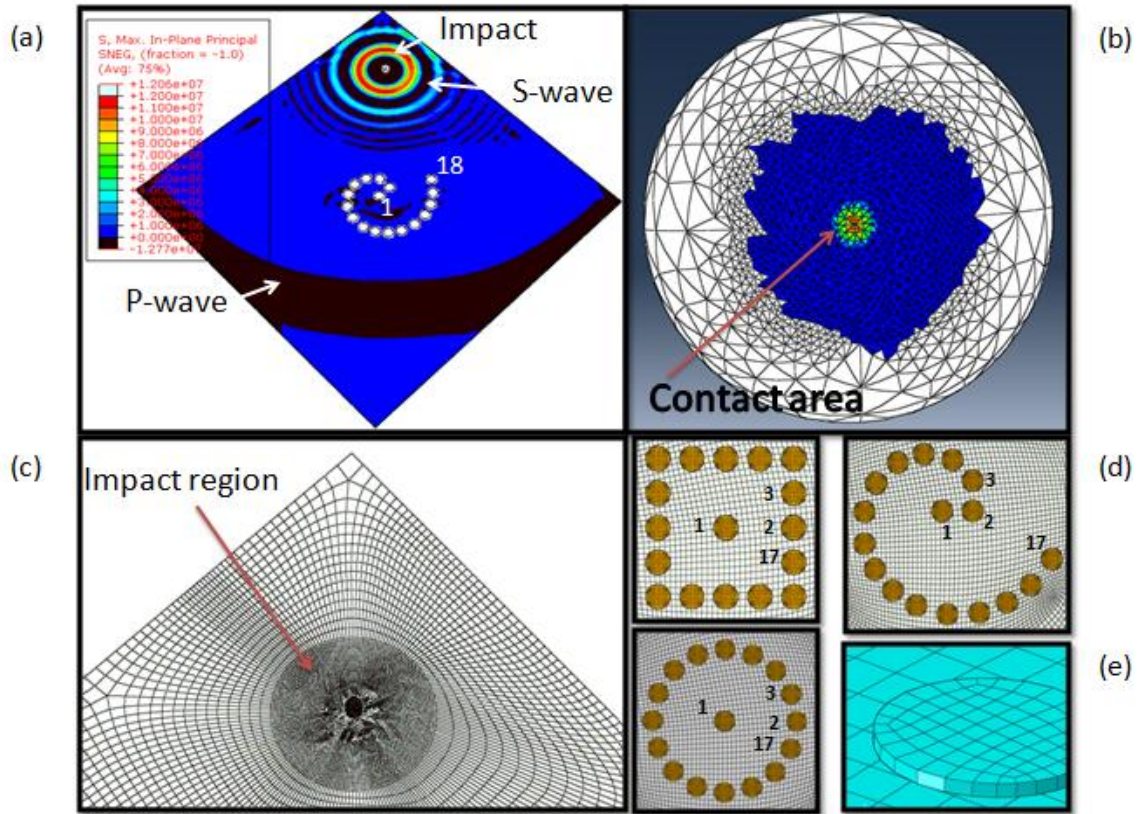
Figure 4.1 CFFEM of a simplified impact event. (a) Excited wave by impact event with in situ TSSC for data acquisition (b) Model of impactor emphasizing the contact area (c) Model of plate emphasizing the impact region (d) Theodorus spiral sensor cluster (TSSC), square sensor cluster (SSC), and circle sensor cluster (CSC). (e) Discrete sensor model emphasizing swift mesh transition ability of tie function in ABAQUS FEM software.

As mentioned earlier, ABAQUS-Dynamic Implicit uses the Hilber-Hughes-Taylor method which is unconditionally stable for a specified range of α-dissipative parameter. In addition to the α-dissipative parameter requirement, it is ensured that the flexural wave frequency was adequately tagged by the simulation time step. A rule of thumb is to have the time step set at 10% of the wave period. As a result, a more than sufficient time step of 1E-6s was stipulated since frequencies of up to 30 kHz was reached. A common approach to control model accuracy is to apply structural damping aka Raleigh damping (an inbuilt function in most FEA packages for simulating structural damping) or apply numerical damping; however, this was not really of essence in the analysis, since it did not affect the trends in the wave signature sought.

4.2 EXPERIMENTAL SETUP TO VALIDATE CFFEM

A simple experiment was performed to replicate the CFFEM and confirm that the signals acquired from the model were a satisfactory approximation of the physical event. Figure 4.2 (a) shows the experimental set-up. The exploded view at the top right of Figure 4.2 (b) show a close shot of TSSC in situ for AUS reception and the denoted sequential numbering of the discrete sensors. The same set-up as modeled in ABAQUS was constructed in our laboratory. A 5 mm diameter stainless-steel solid ball impacting a (610x610x1) mm thin Aluminum 2024-T3 plate embedded with TSSC was tested. The TSSC consisted of 18 discrete sensors sequentially placed at the center of the plate (the 18th sensor was not modeled in ABAQUS and should be ignored). Each individual sensor of the TSSC was placed carefully in the same locations as in the CFFEM. The boundaries of the plate were fixed with a clamping mechanism. The ball was released by

an electromagnet ball holder at a drop height that imposed the same impact velocity as simulated in the CFFEM. A calibrated guide rail system ensured that the ball impacted at the same location and with the same impact energy. A separate 20 mm diameter APC-850 PZT sensor was embedded directly underneath the plate at the impact point. This separate sensor served as a force sensor and was larger than the discrete sensors in the TSSC. In total there were 19 discrete sensors embedded on the plate, one of which was redundant. The larger diameter force sensor was required in order to capture the impact region and consequently the transmitted force history for understanding the dynamics.

AUSs TSSC were acquired via NI PXI-5105 Module (8 channel, 60 MS/sec digitizer). A trigger level was set to begin acquisition at the slightest gain in the force sensor's signal. Due to limited channels, signals from all sensors were collect in 3 batches. The first batch was the force sensor and the first 7 discrete sensors of the TSSC. The second batch was the force sensor and the next 7 discrete sensors of the TSSC. The last batch was the force sensor and the remaining 4 discrete sensors in the TSSC. The force sensor signal acquired in all batches served as a measure to ensure that the excitation level was kept the same during acquisition. Altogether, a total of 18 useful sensor signals were collected from the experiment; 17 from the discrete sensors in the TSSC and 1 from the force sensor. Later in the section 4.3, we shall compare these sensor signals to CFFEM simulation. The transmitting force sensed by the force sensor in the experiment is compared to the contact force output obtained from the ABAQUS CFFES. To do this, the force history signal from experiment as voltage history was converted to force using conservation of momentum law and impulse equation, surmised to give

$$mv_0 = a \int_0^{t_p} V(t)dt \quad (4.5)$$

where m and v_0 are the impactor mass and velocity at impact, respectively, a is a proportionality constant, t_p is the time at peak voltage and $V(t)$ is the voltage signal [76]. Although not all momentum is conserved to the sensor location, equation (4.5) will serve as fair approximate for the force sensor calibration.

(a)   (b)

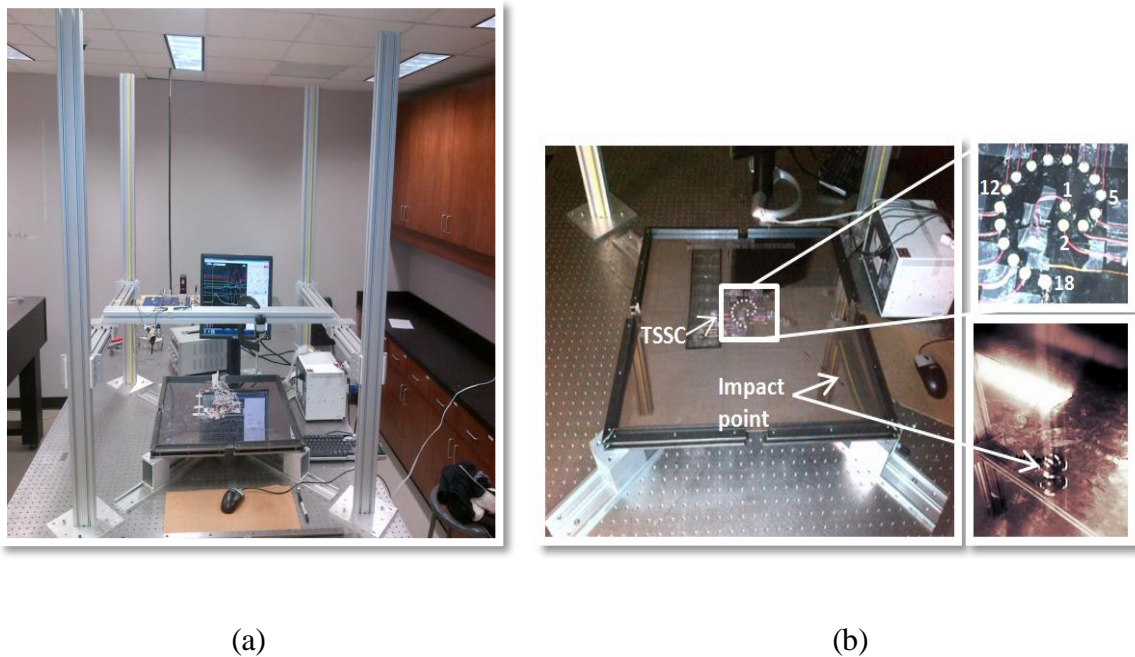Figure 4.2 Experiment setup of idealized impact event (a) Guide rail system (b) Magnified views of plate, TSSC, and impact event

4.3 EMPIRICAL VALIDATION OF CFFEM

In this section, the CFFEM results are compared to experimental results. First, the force history from CFFEM is compared to experiment. Then the time-amplitude electrical potentials as well as the frequency content acquired from the piezoelectric sensor cluster

in the CFFEM are also compared with experiment. We begin empirical validation at the point of impact. Data from CFFES for a stainless steel impactor (5mm in diameter) impacting the aluminum plate with an impact velocity of 3m/s is compared to experiment. The force sensor signal from experiment is calibrated using equation (4.5) and compared to the contact force output from ABAQUS. The "force packet-width" is denoted as the time taken for the collision, pressure exertion, and restitution of the impactor. The results can be seen in Figure 4.3 (a). It can be seen that a very good agreement is found between experiment and CFFES, especially in the force packet-width. The slight discrepancy witnessed is expected and is as a result of the scope of data acquisition in the conducted experiment. In the experiment, it is impossible to place the force sensor at the plate-impactor interface where the impact force is directly exerted. FEM simulation, on the other hand, captures this hidden interface and reports the dynamics more accurately. The contacting elements are surface to surface discretized and a penalty method that accounts for constraint enforcement and shell thickness is adopted [30, 74]. As a result, the peak time force obtained from experiment is slightly delayed by about 1 μs compared to the peak time force obtained from simulation. With an impulse through-thickness transmission speed estimated as the P-wave speed, the 1 μs recorded delay is postulated to be due to a 3 mm misalignment from the impact point, which will include the plate thickness and any small impact point discrepancy between experiment and simulation. The total energy from the impact is not conserved in the small distance from the impact interface. It dissipates as small plate vibrations, hence the lower and delayed force peak in experiments. Surely, multiple trials were performed and the same results were obtained. On this note, we conclude that the simulation results are in very

38

good agreement with experiment. Moreover, the excited piezoelectric signals obtained from the in situ TSSC, discussed later, show very good agreement as well.
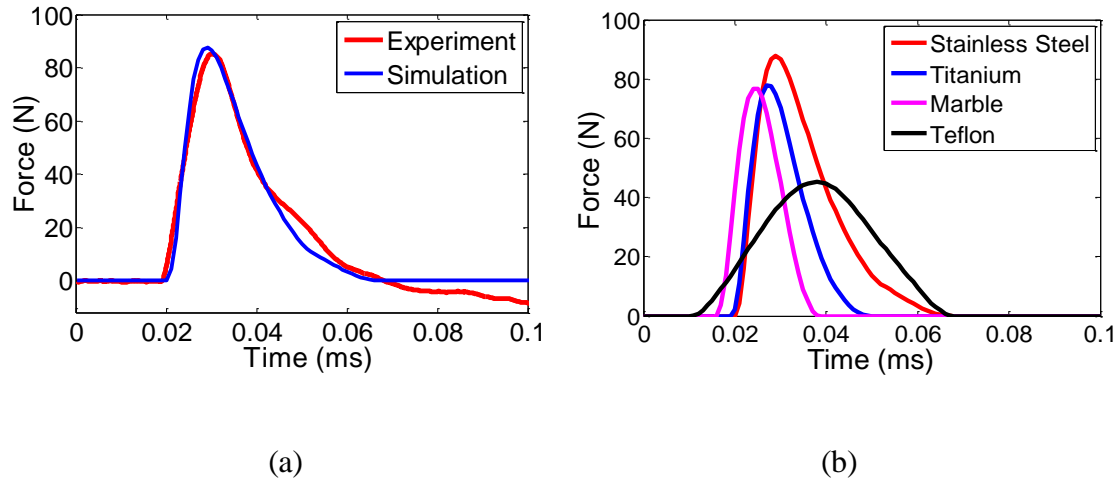
Figure 4.3 Transmitted force history (a) Experiment versus simulation (b) Contact force simulation for various impactor materials

It is expect that an energy dissipation discrepancy would be present in soft materials like Teflon, since soft materials are more prone to viscoelastic energy harvesting and dissipation [72, 76]. Insufficient model parameters which do predict moderate energy harvesting or dissipation leads to unexplainable nonlinearities in the data set. To overcome these nonlinearities we focus on the P-wave packet, since this wave packet consists of the lower modes of the plate vibration. Figure 4.3 (b) shows the contact force histories obtained for all four impactor materials that were simulated including the stainless steel impactor. Correlating impactor mechanical properties with the force profiles obtained from simulation, we find that the elastic modulus and density influences the force packet width as previously observed by Hertz 1882 and several other

39

authors [77, 22-31]. The soft polymeric impactor Teflon has a slow rate of indentation while the metals and ceramic have a high rate of indentation. The density of the impactor correlates with restitution. The higher density materials have slower restitution due to their weight on the plate, except for Teflon which has a slower restitution due to its very low elastic modulus or soft nature and considerable density.

Moving to the TSSC piezoelectric signals as displayed in Figure 4.4, we first identify the details of the data set. It is a time-sensor-amplitude data set. It is not the plate, however, it is the contour map of the stress or strain waves of the plate sensed via the in situ piezoelectric sensor cluster. The piezoelectric signals are induced by the plate's vibrations during and after the impact event. We visualize how the physical waves generate electrical waves in the PZT sensors. The waves are identical and are the class of waves commonly called lamb waves as previously discussed in section 3.1. Lamb wave speeds depend on frequency and mode, hence the phenomenon: dispersion. However, the particular Lamb wave signature excited in this study is the characteristic of the aforementioned class of low velocity, low energy impact event. The waves excited are in particular longitudinal and flexural waves. This hindsight was confirmed by measuring the speeds and frequencies of the wave propagating in the plate. To do this, measurements of the distance and time taking for the wave to travel from one point to the other must be made. For longitudinal wave speed, according to simulation, a speed of 5419 m/s was measured, while experiments reported 5403 m/s. This can be compared with the theoretical value of 5400 m/s previously computed in the section 3.1. The discrepancies in these numbers are expected. They are due to in-exact material properties, material imperfections, and geometry imperfections. Similarly, the flexural wave speed

was measured. From experiment a selected value of 645 m/s was obtained, from simulation: 649 m/s, and from theory using the frequency content obtained from experiment: 668 m/s. For distinguishing the frequency content of each wave type, a STFT of the signal was computed.

(a)   (b)
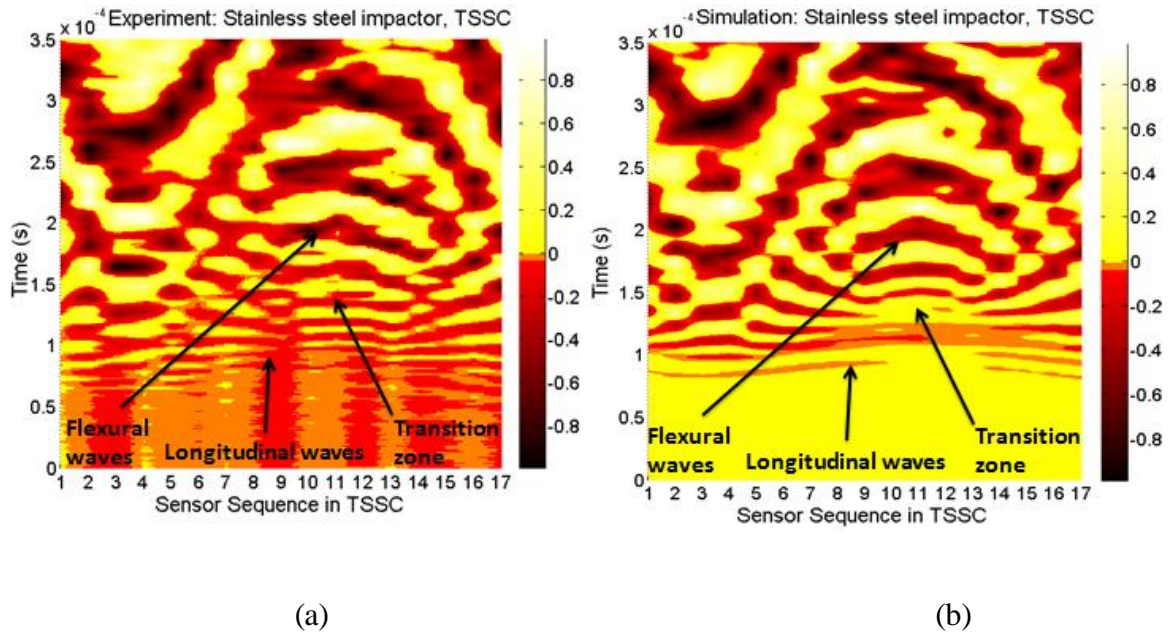
Figure 4.4 Piezoelectric potentials obtained from 17 sensors in the TSSC for a stainless steel impact on plate (a) experiment (b) CFFE simulation

Although the longitudinal wave region in the electrical potential plot generated from experiment (see Figure 4.4 (a)) is drowned in noise, we can see the wave regions clearer from CFFES result (see Figure 4.4 (a)), which is overall in agreement with experiment. The longitudinal wave is the primary wave (P-wave) that transmits first before the secondary wave (S-wave). It appears as the formatted black wave in Figure 4.1 (a) and has a negative stress value, implying the plate region to be in compression. P-waves have greatest speeds and energy, and have the most direct relationship with the impactor elastic moduli. We shall designate two categories of impactors: hard and soft

impactors. Rationally, hard impactors have high elastic modulus in the range 30 to 300 GPa. Similarly, soft impactors have low elastic modulus in the range 0 to 20 GPa. For hard material impactors like stainless steel, titanium or marble, the frequency content is high since they excite more plate waves due to excitation of higher frequencies from a faster rate indentation, while for soft materials like Teflon, Acetal or wood, the frequency content is less. However, these relationships are quite subtle, especially for the rather intermediate impactors (elastic modulus in the range 20 to 100 GPa), and require tuning of the signal window for the effective transmission of the P-wave packet.

(a)   (b)
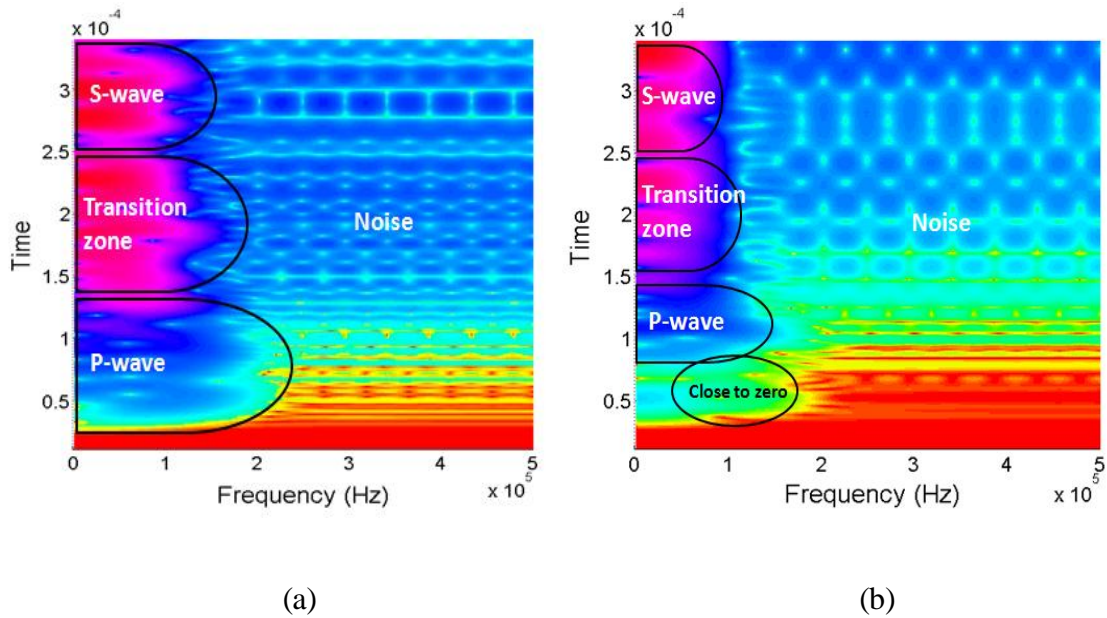
Figure 4.5 Power spectral density of discrete Sensor 1 piezoelectric potential (a) Stainless steel impactor (b) Teflon impactor

The secondary wave or S-wave arrives second, hence the term 'secondary'. In this particular case, it is the flexural wave of the plate. It dominates the signal when softer materials impact the plate. The softer the impactor, yet with an uncompromised impact energy, the lesser the P-wave excited in the plate. However, these trends are highly

42

nonlinear because of the effects such as resonance between the impactor and plate due to coupled material properties, non-linear contact during plate impact, damping mechanisms, boundary reactions, and temperature variation. Figure 4.5 (a) and (b) are the power spectral density plots of a stainless steel and Teflon impactor, respectively. Here, it is shown that while maintaining the impact energy and impactor radius constant, the overall frequency and power spectral density of the plate vibration can be influenced by the impactor material and are generally lower for softer materials

Taking a closer look at the discrete sensors from the TSSC, we compare signals obtained from simulation to those obtained from experiment for a final validation the CFFEM. Figure 4.6 displays the signals for a representative number of sensors. It can be seen that there is a good match with experiments in both time and frequency domains amidst the complexity of the physical problem. Discrepancies in these electric signals are mainly attributed to slight differences inevitable in discrete sensor positions between the CFFEM and experiment model. Shifts in dominant frequency can be observed when matching from the 1st to the 12th sensor FFT plot. This enhanced frequency band sensitivity is the nature of TS geometry and surmounts to the conceptualization of the DFB feature extraction technique that will be discussed later in section 5.1. Next, a side by side evaluation of CSC, SSC and TSSC is conducted to compare frequency sensitivity and judge the efficacy of the spiral sensor cluster to classifying the impactor materials.

4.4 TSSC VERSUS CSC AND SSC

In this section, TSSC is compared to two conventional sensor clusters, which are the CSS and SSC. One fact to note is that TSSC has more angle variation than CSS or
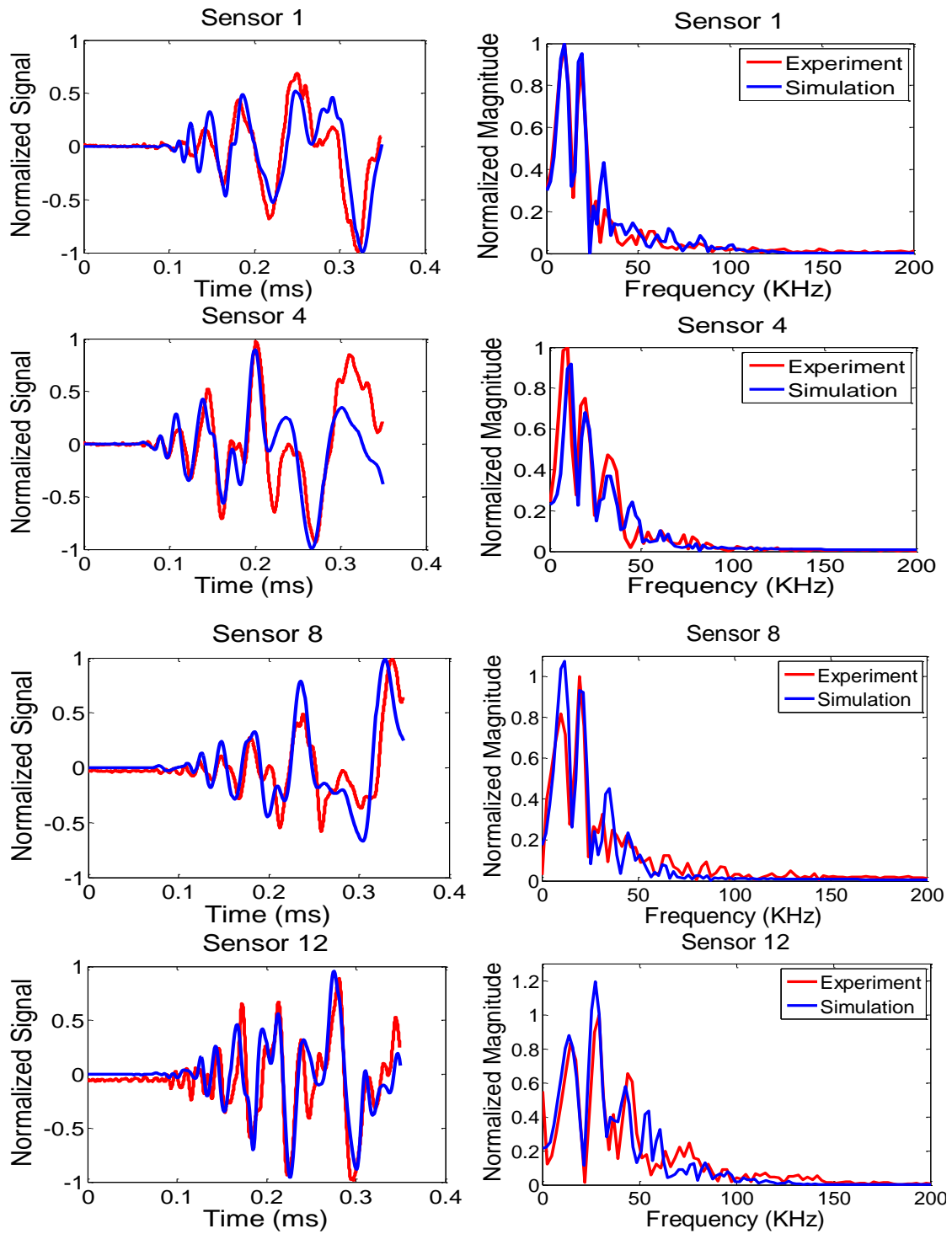
Figure 4.6 Piezoelectric signals from discrete sensors 1, 4, 8 and 12 (right column) and their respective FFT (left column), obtained from both experiment and CFFE simulation of a stainless steel impactor event.

SSC (recall Figure 2.1 (a) or equation (2.1)). This means that for a given circular wavefront with modes k undergoing low dispersion, TSSC will capture more $k_x = k\cos\theta$ and $k_y = k\sin\theta$ components of the wavefront than CSS or SSC. TSSC sees more wave modes and consequently is more sensitive to the AE frequency content. In essence, TSSC hears sounds better. We can witness this subtly in time domain when comparing the electrical potential contour maps of CSC and SSC respectively displayed in Figure 4.7 (a) and (b) to that of the TSSC previously displayed in Figure 4.4 (b). It is clearly noticed that the first longitudinal wave packet that transmitted through the sensor clusters for a relatively shortest time of 12 μs at the 80 μs marker is coarsely generated in the CSC or SSC contour maps but finely generated in that of TSSC. Likewise but subtle are all other waves coarser in CSC and SSC contour maps than TSSC's. The finer contours in TSSC plot means that TSSC has enhanced frequency resolution in its AE reception.

(a)   (b)
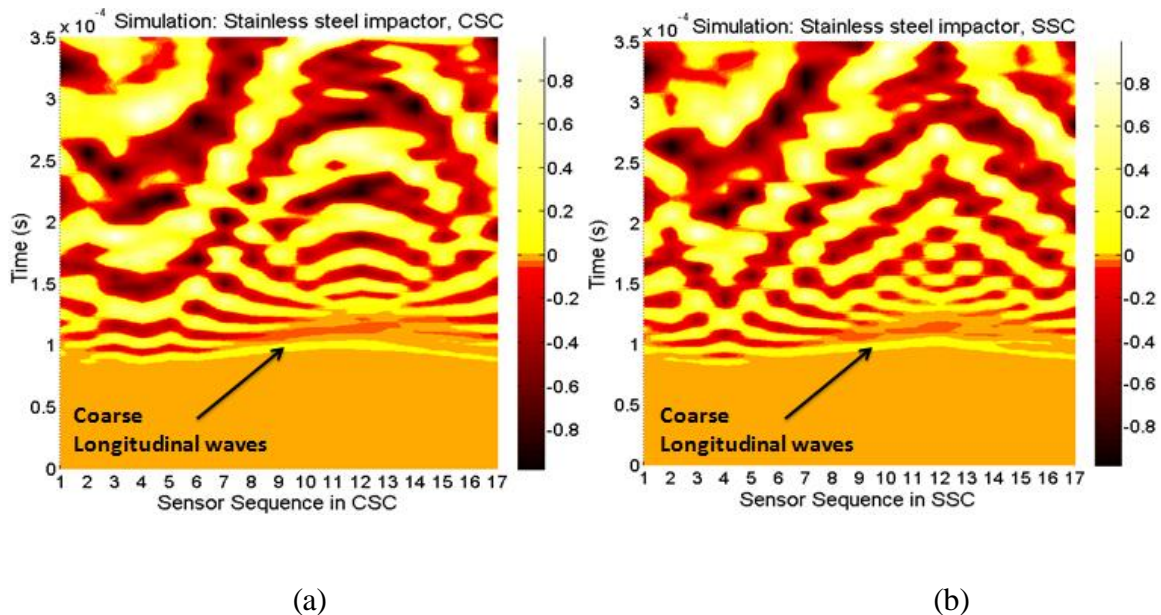
Figure 4.7 Piezoelectric potentials obtained from CFFE simulation from all 17 sensors for a stainless steel impactor event (a) CSC (b) SSC.

CHAPTER 5

FEATURE EXTRACTION FOR IMPACT EVENT CLASSIFICATION

Overview

In this section, a physics-based feature extraction approach is implemented to investigate the AUS relationship with impactor material and corresponding force history. The original AUS is reduced by extracting meaningful features that are then used for impactor material classification. This will be useful for the eventual reconstruction of the probable force history of the impact event. As discussed earlier, the unique solution for the Lamb waves generated by a random elastic impact event on plate is indeterministic. Moreover, this is the forward problem. The backward or inverse problem becomes the problem of solely using the AUSs from the impact event to obtain probable impact parameters and force history. For this purpose we require knowledge from the physics of Lamb waves in relation to key parameters of the impact event. Feature extraction techniques are then developed as a means for classifying the impact event parameters. Since the solution of the inverse problem is not encapsulated in a single technique or model [78], we combine the physics-based feature extraction techniques with theory to formulate a master approach for force history prediction. We introduce the dominant frequency band (DFB) and lag index (LI) feature extraction techniques in this chapter. First, the cluster configuration effect on DFB is isolated to investigate the efficacy of TSSC over CSC and SSC in the classification of impactor materials. Then feature extraction techniques are examined as a function of the impactor materials.

5.1 DOMINANT FREQUENCY BAND

Dominant frequency is the key feature for signal contraction of this type [79, 80]. It captures the subtle deviations in transient elastodynamics due to the plate-impactor material coupling. This succinct yet useful technique is able to classify the impactor elastic modulus as well as qualify the sensitivity of the sensor cluster to frequency content of the AE. A DFB extraction algorithm is written in MATLAB to process the AUSs. The DFB algorithm passes the arrays of AUSs $A(t)_{i,j,k}$ through a low-pass filter, a normalization function, and a P-wave windowing function. After which it takes both the classic Fourier transform (FT) and short time Fourier transform (STFT) of the processed signals and then extracts the peak magnitudes from the outputs of both transforms. The peak magnitudes are used to identify the transient dominant frequencies transmitting in the plate due to the impact energy flow. These dominant frequencies are compiled for every ith discrete sensor in the jth cluster with respect to the kth impactor. It should be noted that DFB technique is applied to the P-wave packet of the signals in order to capture meaningful information and also avoid boundary reflections. A schematic of the DFB algorithm is shown in Figure 5.1. DFBs computed from FT are compared to DFBs computed from STFT in parallel. The FT aka fast Fourier transform (FFT) and STFT techniques are briefly discussed next.

FT aka fast Fourier transform (FFT) is a fundamental signal processing algorithm that computes the frequency content of a signal. The transform takes the signal as input, in this case a transient signal, and decomposes it in terms of sinusoidal frequencies. Mathematically, a transient signal $A(t)$ has the FT given by

$$X(\omega) = \int_{-\infty}^{+\infty} A(t)e^{-j\omega t}dt, \quad -\infty < \omega < \infty \quad (5.1)$$

where ω is the frequency.

STFT operates with a windowing function that preserves the time information of the signal while computing the FTs. Time resolution is at the cost of frequency resolution and vice versa. A spectrogram of the signal can be obtained by computing the power spectral density $H(\tau, \omega)$ at time τ in the form

$$H(\tau, \omega) = |X(\tau, \omega)|^2 = \left| \int_{-\infty}^{+\infty} A(t)w(t)e^{-j\omega t}dt \right|^2. \quad (5.2)$$

This matrix connects the time and frequency information of the signals, and is processed for peak magnitudes which correspond to dominant frequencies.
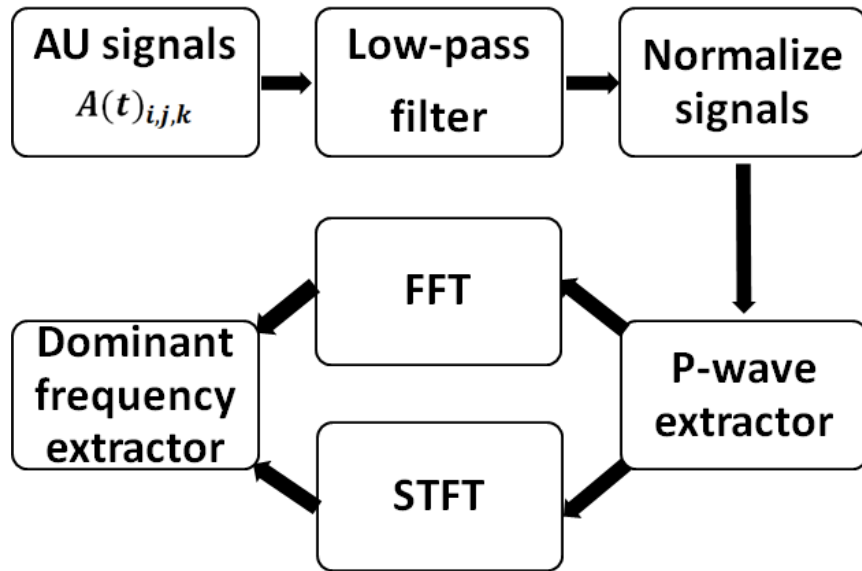
Figure 5.1 Schematic of DFB feature extraction algorithm

5.2 DFB TEST ON CFFEM SIMULATED DATA

From CFFES AUSs, DFB relationships can be plotted for TSSC listening to the stainless steel, titanium, marble, and Teflon impacts. Similarly the same relationships can be plotted for CSC and SSC listening to the same range of impactors in order to investigate the effect of the sensor cluster and classify the impactor as well. We look for positive covariation through the proposed feature extraction technique and sensor clusters. Again, the material property variation in correlation to the DFB is subtle. In order to capture the physics that will distinguish the impactor elastic moduli, we focus on the P-wave packet of the wave signal since it is observed that the P-wave encapsulates the lower modes of the wave that better represent a positive covariation in elastic modulus and DFB. Figure 5.2 shows the P-wave DFB for the four impactor materials with respect to the in situ sensing platform. Already observable are the higher dominant frequency values of the individual discrete sensors when compared with the FFT plots in Figure 4.6. This is because the P-wave packet contains the highest frequencies. The plots agree with the rationale that hard impactors excite higher frequencies than soft impactors. We can see that the soft nature of Teflon impactor excites the lowest DFB. This is true for all clusters. Next is marble and titanium with intermediate hardness and DFBs. Noticeable is the ability of TSSC to sense a variety of frequencies compared to CSC or SSC. This is more obvious in stainless steel and titanium impactors, since they excite more frequencies. Most importantly observable is that TSSC is able to distinguish not only Teflon and marble impactors, but able to distinguish stainless steel and titanium impactors as well. It can be seen that TSSC better distinguishes stainless steel from titanium and marble impactors by a more consistent or rather quantifiable differences. Whereas such differences are almost absent in the data derived from CSC and fully

49

absent in data derived from SSC. This validates the robust sensing capabilities of TSSC over CSC and SSC. The DFB obtain from TSSC using FFT slightly does a better job in distinguishing the impactor materials than its STFT counterpart. This is because in FT the entire signal is sampled as a whole and not in windows; hence, no frequency information is compromised.
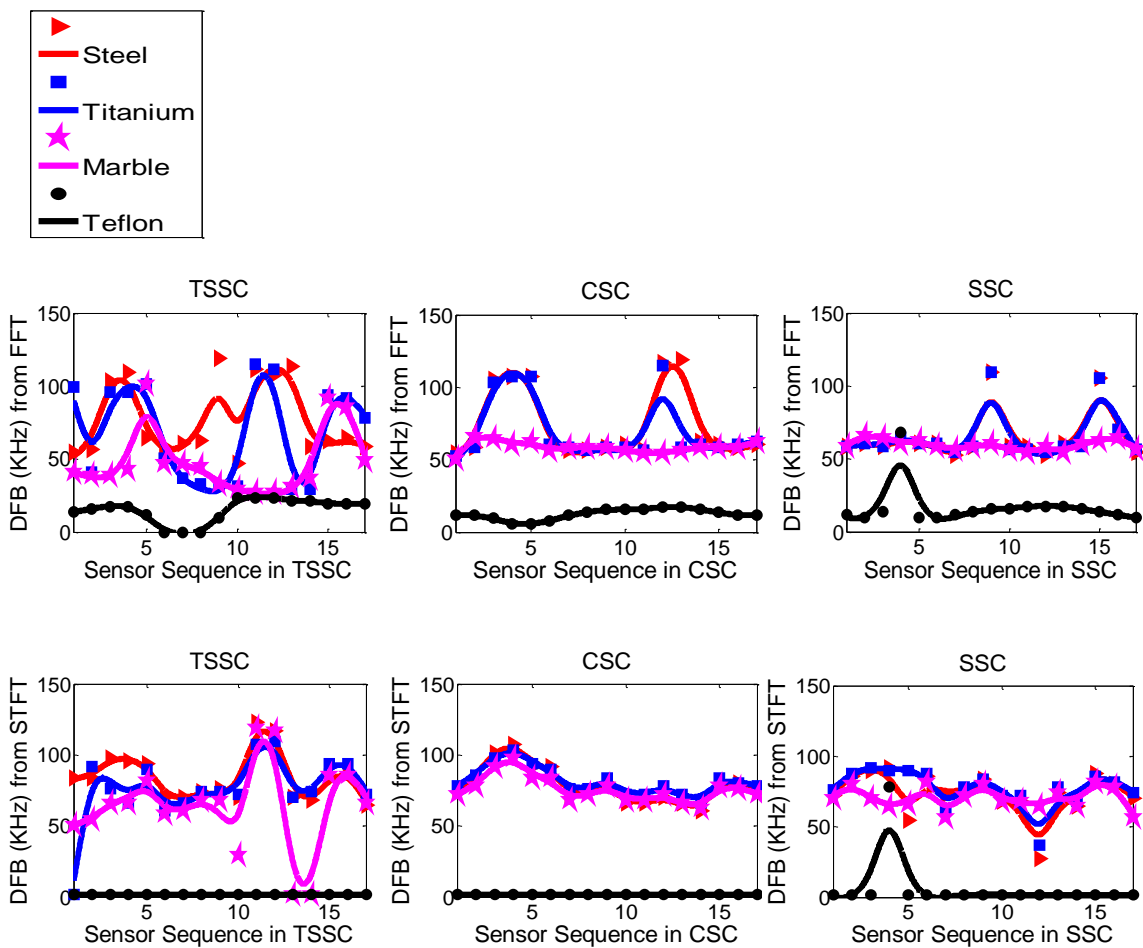
Figure 5.2 DFB of pressure wave packet for chrome, marble, and Teflon impactors sensed with SSC, CSC, and TSSC

5.3 LAG INDEX

The lag index (LI) is directly related to the time delays in the AUSs transmitting between paired sensors in the cluster. It is obtained for the duration of the impact event or preceding the impact event, and can be further related to the elastic wave frequency and speeds excited in the plate during the impact. From Lamb wave theory, we expect that lag coefficients are proportional to the speeds of the wave, given that the lower frequency AUSs generate bigger lag coefficients. LI is obtained as the cross-correlation function with a mathematical expectation defined by

$$L = \sum_{i=1}^{n} 1 - x_t^r x_{t-\varphi}^j W(t), \qquad (5.3)$$

where x_t^r are the AUSs of the reference discrete sensor, $x_{t-\varphi}^j$ are the AUSs of the correlated discrete sensors as a function of phase lag, φ and $W(t)$ is the windowing function [81, 82].

5.4 TSSC-DFB-FFT AND LI TECHNIQUE VALIDATION WITH EXPERIMENTAL DATA

The conducted experiments in the previous section validated the CFFEM, while the simulations justified the redefined AUS feature extraction technique, namely TSSC-DFB-FFT, as a basis for impactor elastic modulus classification. For a validation of this hindsight, yet another experiment is conducted. In this experiment, a new set of impactors with equal diameters (12.7 mm) and a new aluminum plate, 610x610x1 mm in dimension (approximately double the size of the previous) was used. Again, the impactors where controlled to impact the plate at equal impact energy and the P-wave packet was

considered for a linear correlation. The TSSS-DFB-FFT combination was used for best results. Figure 5.3 shows a compilation of the results.

Figure 5.3 A compilation of TSSC-DFB-FFT technique validation results (a) Force profiles due to the impactors (b) Typical AU signal obtained from sensor 1 in clus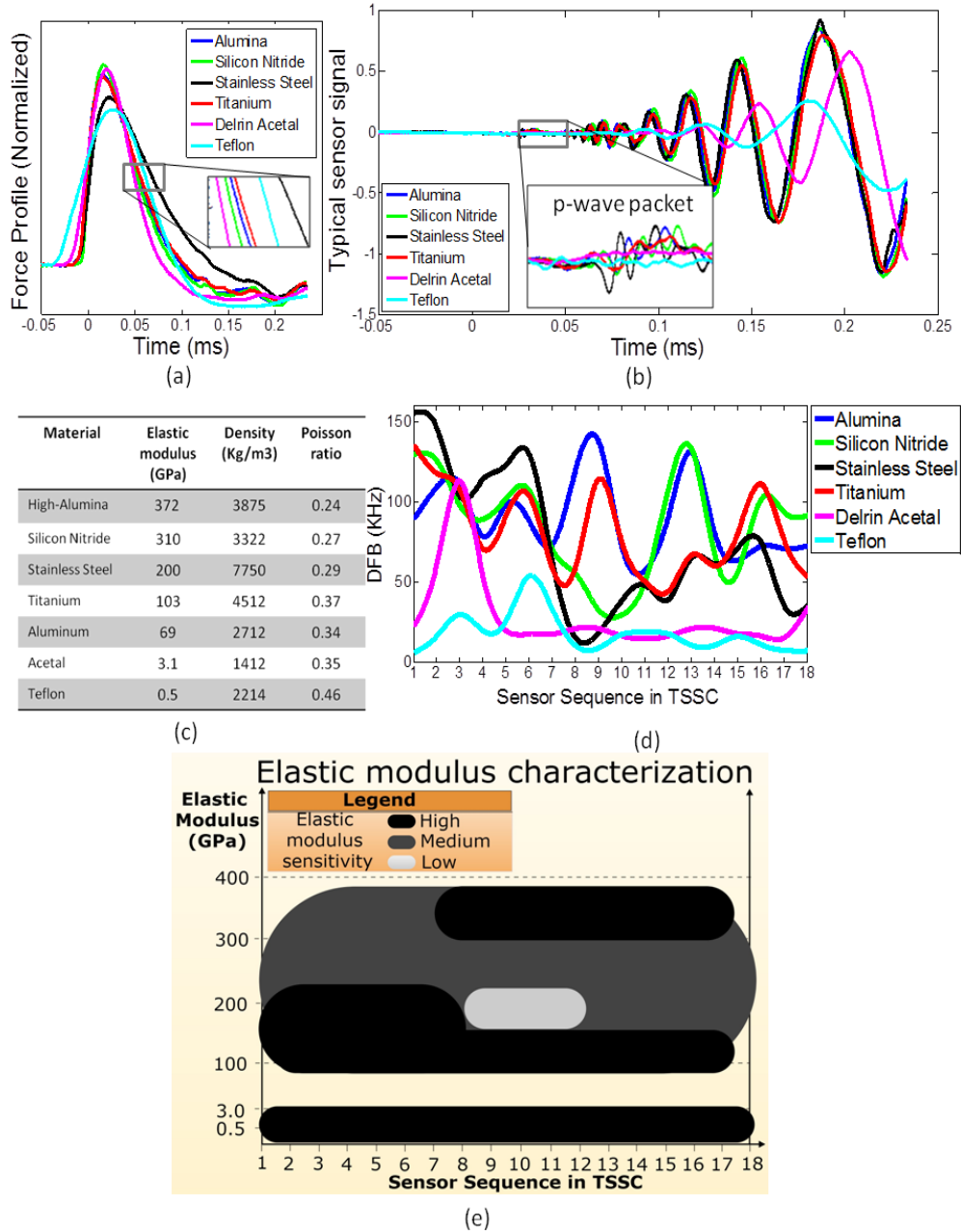ter (c) Material properties of employed specimens (the values reported are standard specifications that were optimized by experiments and finite element simulations) (d) DFBs due to the impactors (e) DFB sensitivity to impactor elastic modulus chart

Correlating impactor mechanical properties with force profiles according to Figure 5.3 (a), we find that the elastic modulus affects the impactor rate of indentation. The relatively low elastic modulus materials (i.e. Teflon, Delrin Acetal, and Titanium in increasing order) have a slower rate of indentation. The density of the impactor correlates with restitution. Relatively higher density materials like Stainless Steel and Titanium have slower restitution. This in turn implies that there is more quasi-plastic deformation in the plate due to the weight of the impactor. However, Teflon has a slower recovery earlier in the restitution process than titanium, silicon nitride and alumina due to its very low elastic modulus or polymeric nature and considerably significant density. Delrin Acetal, having the lowest density, has the fastest restitution. The force profiles have no observable dependence on the Poisson ratio of the impactor. Correlating the mechanical properties with the AU signals and DFBs, we find that higher elastic modulus and high density materials like Alumina and Stainless Steel excite higher frequency and consequently higher DFBs in the sensor cluster. However, coupled mechanical properties of the plate and impactor can induce a discrepant or nonlinear effect as can be slightly seen with titanium having high dominant frequencies at sensors 1, 9 and 16. This effect is similar to resonance. Other sources of non-linear covariation between elastic modulus and DFB may be caused by dead zones in the form of vibration nodes that remain stationary due to the plate mode.

Figure 5.4 displays the Lag coefficients obtained from processing respective time-domain-segmented AUSs from all discrete sensors in TSSC as excited by the various impactor materials. A Hann window was used for the time domain data segmentation. It can be observed that the elastic moduli of the impactors are linearly classified most

53

especially in the impactor transmission time window that spanned approximately 0 to 0.2 ms (see Figure 5.4 (a)). During this time, Delrin Acetal and Teflon impactors are distinctly classified. However, for the time window spanning 0.2 to 0.4 ms after the impact event is complete, the soft impactors are no longer distinctly classified and the order of the impactor materials with respect to increasing LI is reversed (see Figure 5.4 (b)).

(a)   (b)
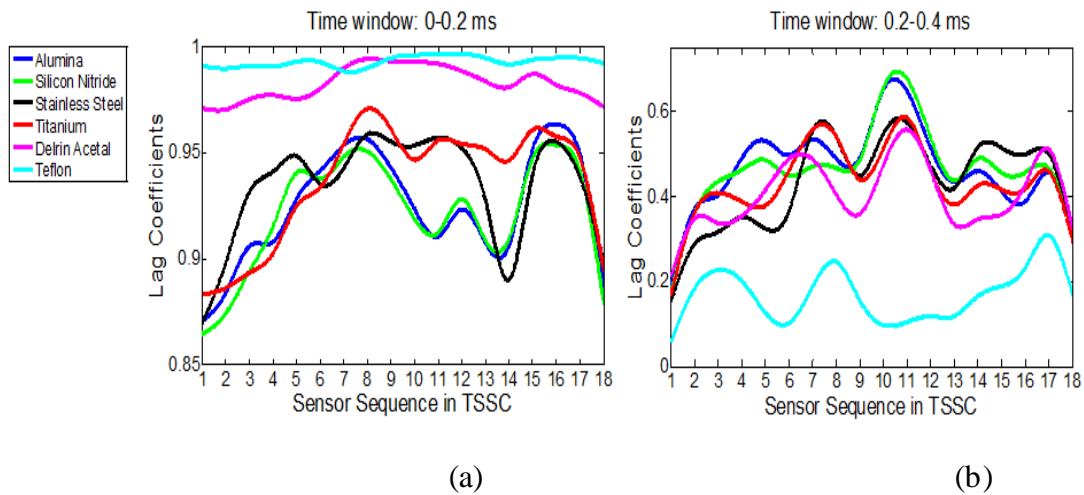
Figure 5.4 Lag coefficients obtained from TSSC due to the range of impactor materials exciting AUSs for the time window of (a) 0-0.2 ms (b) 0.2-0.4 ms

5.5 PARAMETRIC MODEL STUDY FOR FORCE PROFILE PREDICTION

Figure 4.1 (a) showed the first symmetric and anti-symmetric wave modes (i.e. P-wave and S-wave) simulated in the plate, traveling towards TSSC. This wave packet captured in the snap shot provided best results when performing DFB and LI analysis. In essence, the wave excited during the impact which spanned approximately 0 to 0.2 ms provided better results than subsequent waves. For our particular analysis, sensors 1 to 18, sequentially denoted in Figure 4.2 (b), were cross-correlated with sensor 1 to obtain

the lag coefficients. In essence, sensor 1 was auto-correlated. DFBs and LI from experiments were directly correlated with β and γ simultaneously, and both FETs served as impactor classifiers that activated the modification parameters in a CZ formulated algorithm. Hence, solutions for the case of 'soft impactors' (i.e. Delrin Acetal and Teflon) where corrected. Highest LI and lowest DFB identify Teflon, and then appropriate weights on β and γ obtained from best fitting are activated. A similar correlation is done for Delrin Acetal. This enables better force history solutions for soft impactors, computed using CZ theory. Without this, the solutions for the soft impactors are exaggerated as can be seen in Figure 5.5 (a).

The force history signals from experiment as voltage histories were converted to unit of force using equation (4.5). By directly linking force histories from experiments to CZ theory with empirically derived indices from DFB and LI AUS processing techniques, we found that the values of β and γ for best and consistent fit in the time domain for Delrin Acetal impactor were $(\beta, \gamma) = (3.0 \pm 0.5, 2.50 \pm 0.05)$ and for Teflon impactor were $(\beta, \gamma) = (4.0 \pm 0.5, 0.70 \pm 0.05)$. Force histories obtained from original CZ theory, experiment, and modified CZ theory are displayed side by side in Figure 5.5. It can be seen that the exaggerated transient force histories obtain from original CZ theory (see Figure 5.5 (a)) for soft material impactors are modified (see Figure 5.5 (c)) based on the understanding obtained from experiments (see Figure 5.5 (b)). In addition, the force peaks of the profiles where modified using a universal ς and ε value found to be $(\varsigma, \varepsilon) = (1.50 \pm 0.10, 1.460 \pm 0.005)$ for best matched results. Notice that the dissipation parameter γ and solution time discrepancy parameter β depend on the impactor material. Delrin Acetal has a higher γ-parameter than Teflon because, as

physically witness in our lab experiments although not measured, its restitution coefficient is significantly and visibly greater than Teflon's. Delrin Acetal impactor behaves like a tennis ball, restoring a significant amount of energy during impact which other impactor materials transmit to the plate. On the other hand, Teflon has greater β-parameter due to its soft polymeric nature that is quantized by its low elastic modulus. Inspecting equation (3.15) and (3.18), it can be observed that a low elastic modulus will lead to divergence of the solution in the time domain, resulting in the need for the β-parameter to mitigate the mathematical bias.

(a)   (b)   (c)
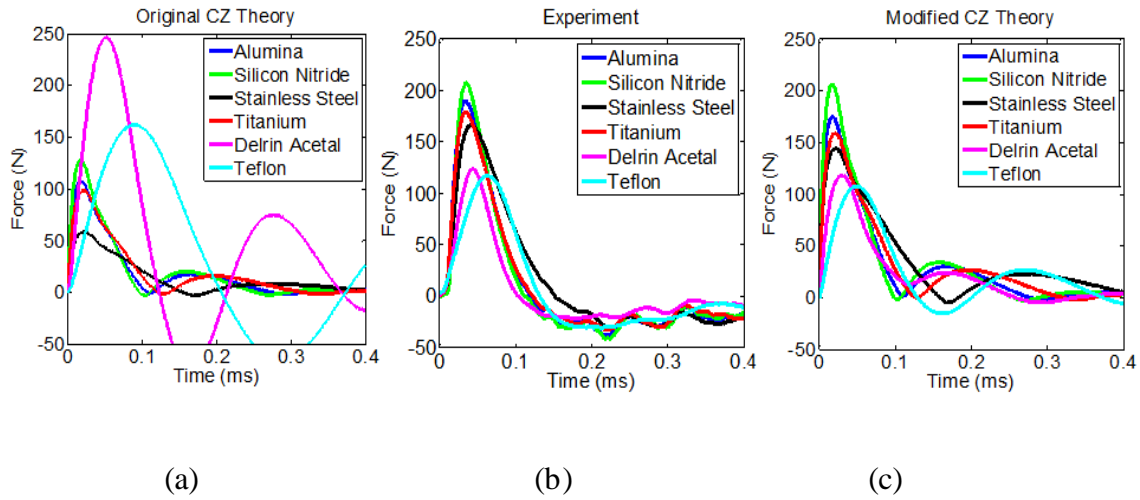
Figure 5.5 Transient force histories obtained for the range of impactor materials from (a) Original CZ theory (b) Experiments (c) Modified CZ theory

CHAPTER 6

Probability Map of Impact (PMOI)

PMOI determines the most probable region of structure where the impact event occurred. By discretizing the impacted structure into small pixels and computing a representative POI for each element, the impact location can be identified based on a probability map instead of a single estimated value. As mentioned earlier in chapter 1, PMOI is an alternate technique for locating the impact region and classifying the impact type. Its profile can be used as an indicator of the type of impact that has occurred. PMOI is developed to be utilized in conjunction with TSSC.

6.1 PMOI EXPERIMENTAL SETUP

An experiment to test the PMOI technique was conducted on an isotropic plate (aluminum plate) of 24 in×24 in. Eighteen (18) piezo-electric sensors were adhesively bonded with the surface in TS orientation (see Figure 6.1). As previously discussed, TS is a special type of orientation for sensor clustering. It starts with an isosceles right triangle with each leg having a length of unit distance. Then another right triangle is formed, an auto median right triangle, with one leg being the hypotenuse of the prior triangle (with length $\sqrt{2}$ of unit length) and the other leg having the unit length. This process is repeated and the i-th triangle in the sequence is a right triangle with side lengths of $\sqrt{i}$ and 1, and with hypotenuse of $\sqrt{i+1}$. For this experiment, the unit distance of 0.5 inch and $i = 18$ were used. The first sensor was placed at the midpoint of

the plate. Then, according to the orientation, all the other passive sensors were placed as shown in Figure 6.1.

Two different objects were used to carry out the experiment. One was a steel ball (~185 GPa) of diameter 0.1905 inch, and the other was a golf ball (~0.3 GPa) of diameter 1.68 inch (see Figure 6.1 (b)). These balls were selected to simulate two different impact types on the plate and each one was dropped at two different impact points to simulate unknown impact locations. The ball drop path was controlled through a vertical pipe designed for each ball and placed above the plate. Drop heights chosen in order to exert suitable impacts on the plate were 18.5 inches for the steel ball and 11 inches for the golf ball. This arrangement accurately controlled the ball drop height and guaranteed that during repeated experiments the ball was striking approximately the same location of the plate with the same energy.

(a)   (b)

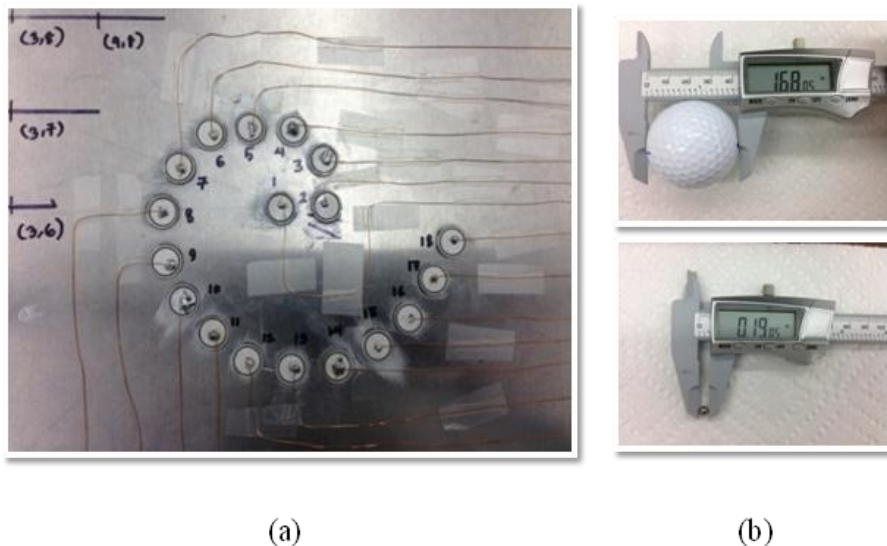Figure 6.1 (a) PZTs mounted on aluminum plate (b) Steel & Golf ball used in ball drop experiment (inch)
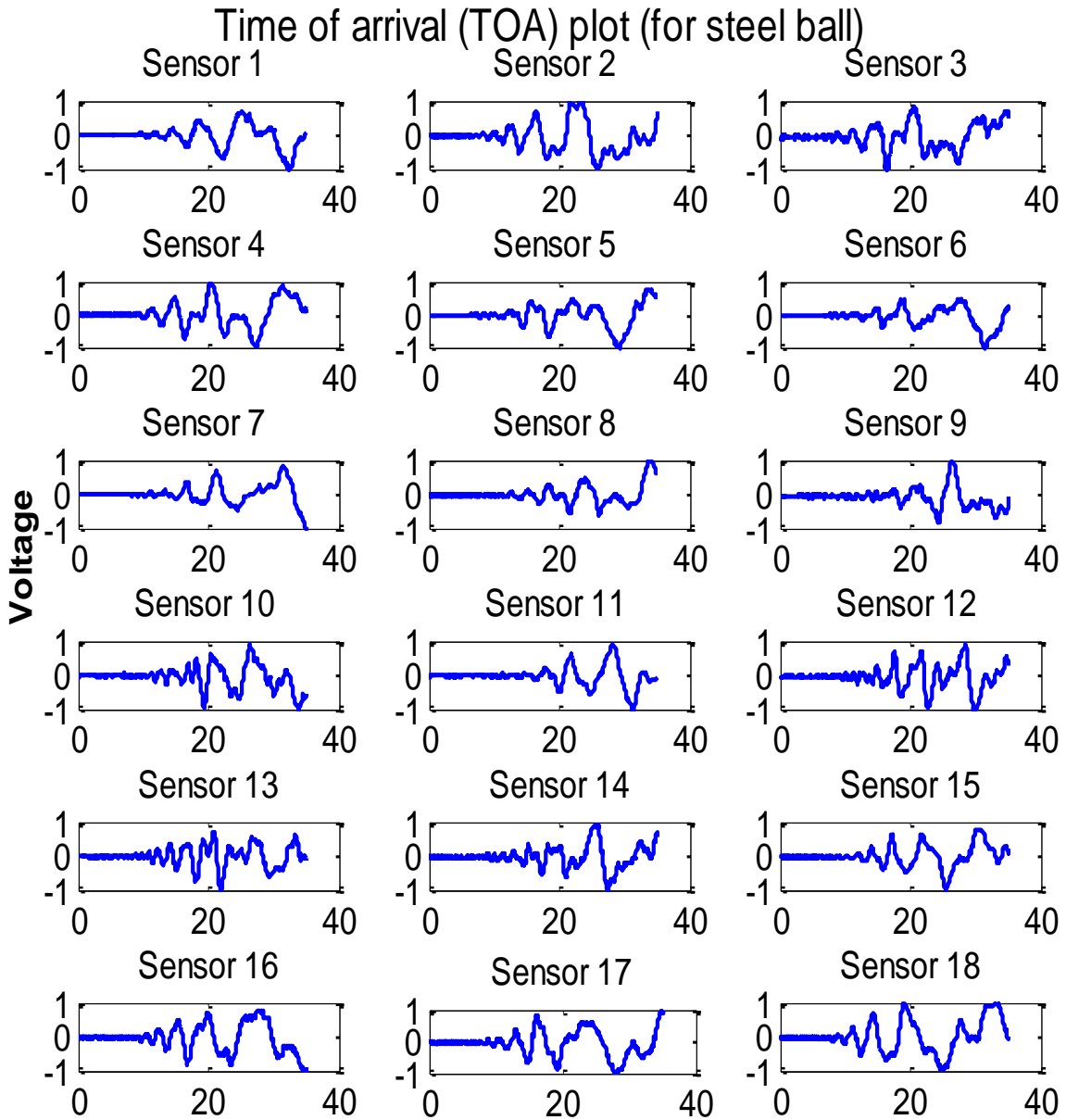
Figure 6.2 Passive signals acquired from all the discrete sensors in TSSC when the steel ball impacts the plate at a distance 5.6 inch from the center of the spiral
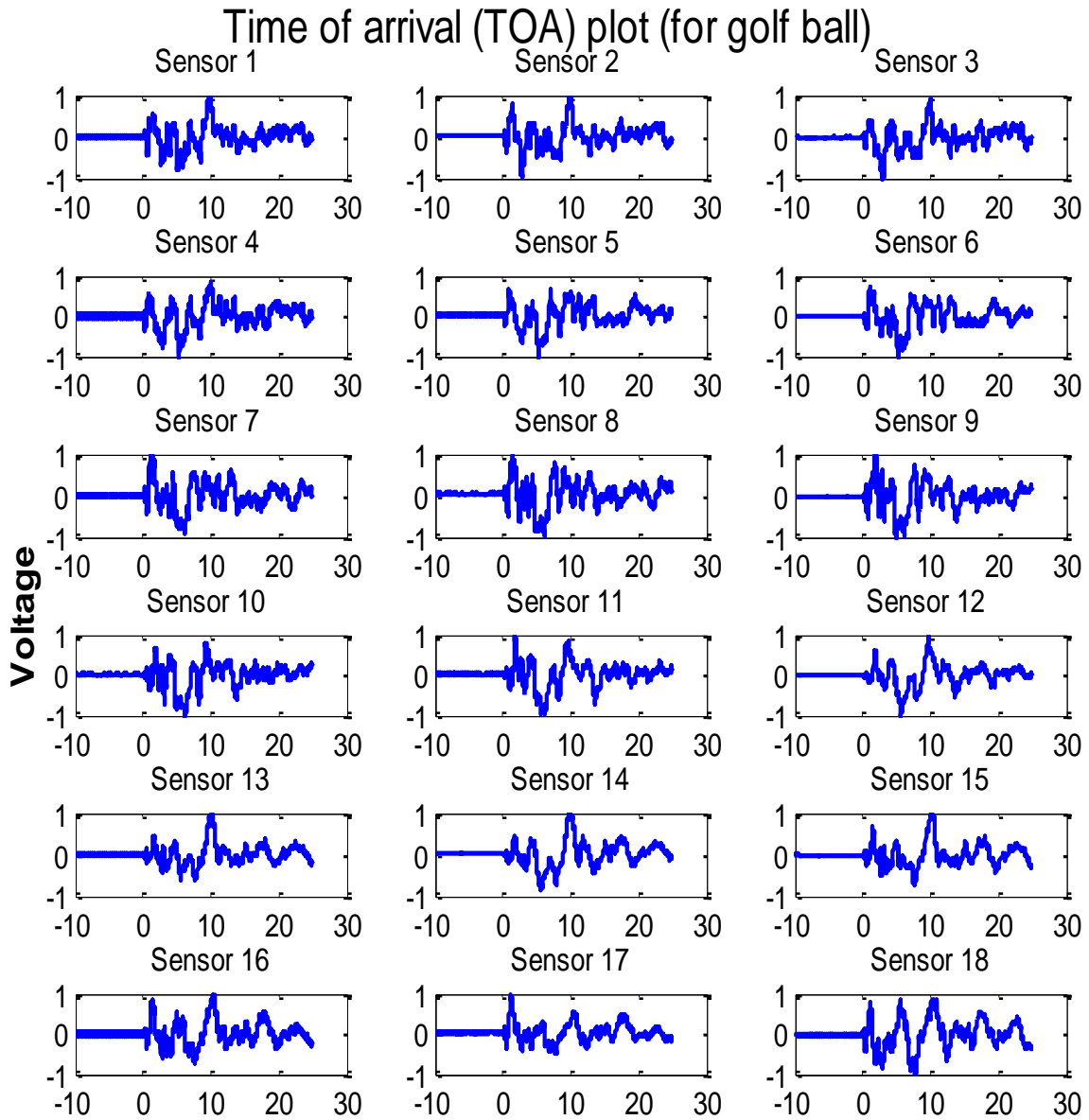
Figure 6.3 Passive signals acquired from all the discrete sensors in TSSC when the golf ball impacts the plate at a distance 5.6 inch from the center of the spiral

Only the middle portion of the plate of dimension 12 inch x 12 inch is considered further for experiment and analysis. Hence, sensor 1 is located at the 6 inch x 6 inch coordinate from the leftmost corner. Repeated experiments were carried out on the plate at 2 different locations, location A: 10 inches x 10 inches and location B: 2 inches x 10 inches from the center of the plate, to predict the impact point from the impact response data. Sensors 1-18 are the locations of the piezoelectric sensors that are placed on the plate. The signals from these sensors were received using NI PXI-5105, 3 8-Ch (3x8<18), 60 MS/sec Digitizer. Simultaneously to re-verify the signals Tektronix TDS 2004C Oscilloscope was used. Sensors were connected with the digitizer using SMB type cable at the digitizer end and SMA type cable at the senor end. A splitter (SMA cable splitter & then SMA to BNC) setup was used to split sensor signals to send to the digitizer and the Oscilloscope simultaneously. This arrangement was used for 4 sensors at a time and all the sensor signals were appropriately verified. Each experiment was conducted at least 10 times to verify for consistent sensor signals.

6.2 TIME OF ARRIVAL ESTIMATION

From the sensor signals, the time of arrival (TOA / TOF) can be obtained manually or through signal processing. It is quite difficult to measure the exact TOA from the time history plot because there is some ambiguity in the plots about the exact TOA or the starting point of the signals. Arrival of the weak extensional mode or the S0 mode is hidden in the low level noise present in the time history plot. Therefore, the exact TOA of the S0 mode cannot be determined. However, arrival times of the relatively stronger flexural mode of the A0 mode can be obtained from the plots by the threshold technique

61

or cross-correlation technique. Using threshold based technique the arrival time of the first noticeable peak greater than the noise level is recorded as the arrival time of the ultrasonic energy. For this analysis both techniques were explored. In cross-correlation technique, the dominant frequency in the signal received in first 150 μs was first obtained at different time windows using Short Term Fourier Transform (STFT) technique. Next a composite tone burst signals of dominant frequencies was created containing 3 cycles for each frequencies at sequential time steps (time windows) as was used in the STFT. A cross correlated signal was then obtained by cross correlating original experimental signal and the composite tone burst signal. First predominant peak observed from the cross correlated signal was selected and designated as TOA. Using thresholding technique, the TOA were also obtained and it was found that they are comparable. The TOA data obtained from cross-correlation technique will be used for further analysis. For more complicated problems, thresholding technique is prone to give error and thus the cross correlation approach is recommended. The cross correlation approach was implemented to find the TOA automatically according to the computer algorithm depicted in Figure 6.4.

Inherently, the differences between actual arrival times of the ultrasonic signals at different sensors are less error prone than the actual TOA at each sensor, if used in the computation for further estimation. The objective function used in developing the PMOI utilizes the differences in the recorded arrival time and thus it is expected to have less error in estimation [50]. However, it has been found that it is still very crucial to obtain accurate TOA because even small errors in TOA sometimes have major effect on the

impact point location determination. In this thesis work two fundamental improvements are proposed.

(1) Use the cross correlation technique and improvement.

(2) Use probabilistic analysis of TSSC sensing data to construct a PMOI rather than define the impact point explicitly.

This will help alleviate problem arising from wave dispersion and error prone selection of TOA. To obtain the PMOI, minimization of objective error function is proposed for better accuracy.
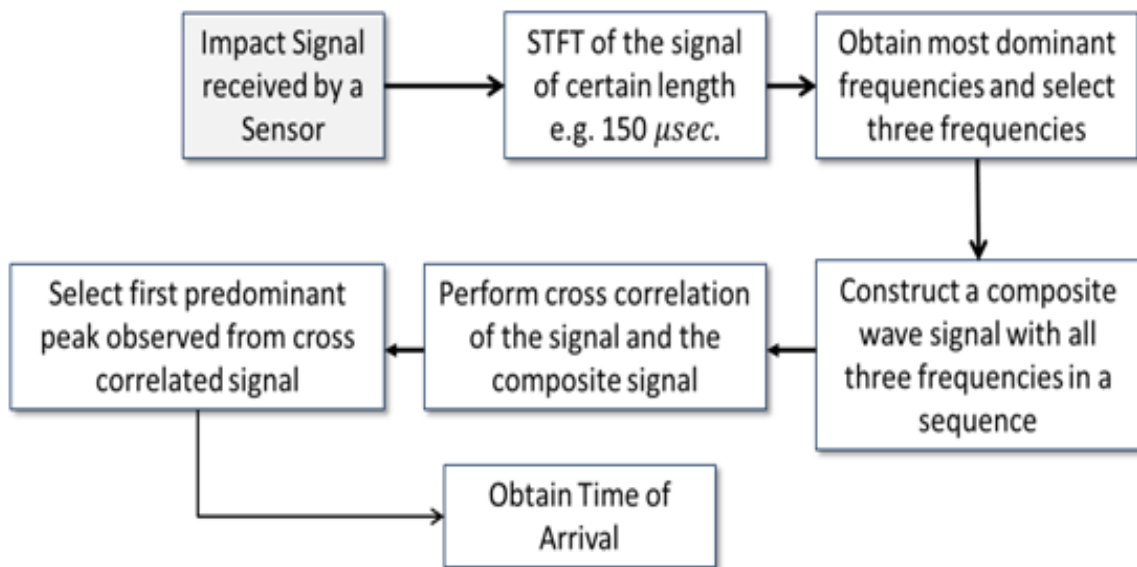
Figure 6.4 A process to describe the selection of appropriate TOA from the impact signal. The TOA obtained from this method closely matched with the TOA values obtained from thresholding technique which is a manual approach that is prone to error and time consuming

6.3 OBJECTIVE ERROR FUNCTION

Sensors arranged in TS are divided in to multiple combinations, keeping at least three sensors in one combination. Hence, one can have $18P_3$ combinations. Although TOAs are obtained from only 18 sensors, all possible combinations could produce multiple error functions to minimize. The structure is discretized into small pixels and all the combinations cast votes to each pixel point. These votes are then used to calculate the PMOI over the entire structure. For details on this technique, let's focus on one combination consisting of three sensors out of $18P_3$ combinations. The time of arrival of the signal at the ith sensor is denoted as t_{it}. If the time of impact is denoted as t_{imp} then the travel time for the signal from the impact point to the sensor location is:

$$t_i = t_{it} - t_{imp}. \qquad (6.1)$$

In equation (6.1) both t_{it} and t_{imp} are defined with respect to the same time of reference. If the co-ordinate of receiving sensor is $(x_i y_i)$, and the impact point coordinate is (x_0, y_0), then the distance of the three sensors from the impact point are given by

$$d_i = \sqrt{(x_i - x_0)^2 + (y_i - y_0)^2} . \qquad (6.2)$$

The time of travel of the wave to sensor locations are denoted as t_i. Considering uniform velocity profile, where the velocity is denoted as c, one can write

$$d_i = ct_i = \sqrt{(x_i - x_0)^2 + (y_i - y_0)^2} . \qquad (6.3)$$

In real life structural health monitoring systems, the sensor location (x_i, y_i) is known; but the impact point location (x_0, y_0) is unknown. If the assumed coordinate values (x_0, y_0) are different from the true impact point, then a positive resulting value of the error function $E(x_0, y_0)$ is obtained. But, if the assumption is correct, then the error function should give a zero value. As the exact time of arrival is often hidden in the

noise, the values obtained from the error function have relatively high error. For this reason, it is desirable that the objective function be expressed in terms of relative times of arrival between sensors instead of the actual arrival times [50] given by,

$$t_{ij} = t_{it} - t_{jt} = \left(t_i + t_{imp}\right) - \left(t_j + t_{imp}\right) = t_i - t_j. \qquad (6.4)$$

A further benefit of this formulation is that it removes the need for explicit knowledge of the time of impact, t_{imp}. Therefore, the relative time of arrival and their ratios are defined as:

$$t_{ij} = \frac{d_i}{c} - \frac{d_j}{c} = \frac{d_i - d_j}{c}$$

$$\Rightarrow t_{ij} = \frac{1}{c}\left\{(x_i - x_0)^2 + (y_i - y_0)^2 - \left(x_j - x_0\right)^2 + \left(y_j - y_0\right)^2\right\}. \qquad (6.5)$$

In a three sensor system, in order to give equal importance to three measurements of arrival times, the error function is defined in a different fashion, after few steps of mathematical juggleries. With this definition of the error function, the impact point location prediction should not be strongly influenced by the experimental error in any one time of arrival measurement.

$$E(x_0, y_0) = \left(\frac{\left\{\sqrt{(x_1 - x_0)^2 + (y_1 - y_0)^2} - \sqrt{(x_2 - x_0)^2 + (y_2 - y_0)^2}\right\}}{\left\{\sqrt{(x_2 - x_0)^2 + (y_2 - y_0)^2} - \sqrt{(x_3 - x_0)^2 + (y_3 - y_0)^2}\right\}} - \frac{t_{12}}{t_{23}}\right)^2$$

$$+ \left(\frac{\left\{\sqrt{(x_2 - x_0)^2 + (y_2 - y_0)^2} - \sqrt{(x_3 - x_0)^2 + (y_3 - y_0)^2}\right\}}{\left\{\sqrt{(x_3 - x_0)^2 + (y_3 - y_0)^2} - \sqrt{(x_1 - x_0)^2 + (y_1 - y_0)^2}\right\}} - \frac{t_{23}}{t_{31}}\right)^2$$

$$+ \left(\frac{\left\{\sqrt{(x_3 - x_0)^2 + (y_3 - y_0)^2} - \sqrt{(x_1 - x_0)^2 + (y_1 - y_0)^2}\right\}}{\left\{\sqrt{(x_1 - x_0)^2 + (y_1 - y_0)^2} - \sqrt{(x_2 - x_0)^2 + (y_2 - y_0)^2}\right\}}\right.$$

$$\left. - \frac{t_{31}}{t_{12}}\right)^2. \qquad (6.6)$$

One shortcoming of equation (6.6) is that for certain values of the unknown (x_0, y_0) the denominator $\left(\sqrt{(x_j - x_0)^2 + (y_j - y_0)^2} - \sqrt{(x_i - x_0)^2 + (y_i - y_0)^2} \right)$ [subscripts i and j take values 1, 2 and 3] can vanish [49]. For those special values of (x_0, y_0) the objective function becomes infinity. Therefore, special care must be taken during the computation of the objective function to avoid these singular points. However, this problem can be easily taken care of by modifying the definition of the error function as described below [50],

$$E(x_0, y_0) = \{t_{23}(d_1 - d_2) - t_{12}(d_2 - d_3)\}^2 + \{t_{31}(d_2 - d_3) - t_{23}(d_3 - d_1)\}^2$$

$$+ \{t_{12}(d_3 - d_1) - t_{31}(d_1 - d_2)\}^2 \qquad (6.7)$$

Using equation (6.7), the pixel points were obtained where the minimum value of the error occurred. Therefore, the impact point location is the point where the error is minimum. Although it is eminent that all combinations supposed to provide very close location of impacts, a sparse distribution of impact point was observed from all the combinations in TSSC. Sparseness of data set was found to be impact type dependent and it was consistently found that the lower frequency content (large and soft impact object with a corresponding large contact area) impacts have wider sparseness in data than the higher frequency content (small and hard impact object with a corresponding small contact area) impacts.

6.4 PROBABILITY MAP OF IMPACT DERIVATION

The objective here is to estimate the probability of impact on the entire structure along with the type of impact using the PMOI technique. After an impact incident, AUSs are obtained and error function values are computed, from which a PMOI is derived.

Hypothetically, each pixel point, according to specified resolution, on the structure is subject to have some degree of probability of being the impacted point. A group of pixel points may have higher probability than other points, vise-versa some points may manifest negligible probability. A 3D probability distribution over the entire structure is useful to visualize the high probability zone. Next the contour graph obtained after considering equal probability lines from the 3D probability distribution plot will provide the understanding of equiprobability zones, thus generating the PMOI. One could easily select a portion of the structure which is inside a desired equal probability line. Say for example, one is interested in investigating a structural region with 98% probability of impact. Then it is obvious from the PMOI that the structural area inside 98% equiprobability line must be investigated. It would be convenient if such PMOI is obtained automatically from the sensor data received after an impact event. Thus the method is described here. The process is to obtain most probable zone of impact on the structure. It is assumed that the variation in the data collected from sensors is due to sampling error (experimental or measurement). The most common probability distribution for modeling measurement error is Gaussian distribution. A bivariate Gaussian probability distribution [83] is suitable for the observed impact point ((x, y) coordinates) obtained after minimizing the objective error function developed in section 6.2. A bivariate normal distribution is determined by the following parameters: the center (mean) (μ_x, μ_y), the spread (standard deviations) of the two coordinates (σ_x, σ_y) and a correlation between the two variables ρ. Specifically, if random variables (X, Y) follow a bivariate normal distribution then the joint probability distribution is given by density function f as follows:

For $-\infty < a < b < \infty$ and $-\infty < c < d < \infty$

$$P(a < X < b, c < Y < d) = \int_a^b\int_c^d f(x,y)dxdy \qquad (6.8\ a)$$

Where,

$f(x,y) =$

$$\frac{1}{2\pi\sigma_x\sigma_y\sqrt{1-\rho^2}} \cdot \exp\left[-\frac{1}{2(1-\rho^2)}\left\{\left(\frac{x-\mu_x}{\sigma_x}\right)^2 + \left(\frac{y-\mu_y}{\sigma_y}\right)^2 - 2\rho\left(\frac{x-\mu_x}{\sigma_x}\right)\left(\frac{y-\mu_y}{\sigma_y}\right)\right\}\right]. \qquad (6.8\ b)$$

For the present study the center of the bivariate normal distribution (μ_x, μ_y) represent the estimated impact point. However, it is not the intention to obtain an exact impact point but the equiprobability zone of impact on the structure. To fit an appropriate bivariate distribution it is required to estimate the parameters $(\mu_x, \mu_y, \sigma_x, \sigma_y, \rho)$ from the TSSC data and subsequently minimized error function coordinate. R software with package "prada" [84] is used to fit appropriate bivariate normal distribution to the observed data and obtain the PMOIs. The data showed noises for some coordinate parts on the structure, which supposed to be away from the true impact point. Even including such noisy points in the analysis, quite accurate estimation of impact region was obtained. Such noises can be easily removed and the data near high concentration area are then emphasized. A built-in scale factor can be introduced for the standard deviation to select the data points to estimate the parameters $(\mu_x, \mu_y, \sigma_x, \sigma_y, \rho)$. In this thesis work, the utilization and adoption of such scale factor is not discussed in details. Such parameters could be function of material, sensor combination, impact type and the environment and such effects are under study and here the discussions are omitted.

6.5 COUPLED FIELD FINITE ELEMENT SIMULATION FOR PMOI
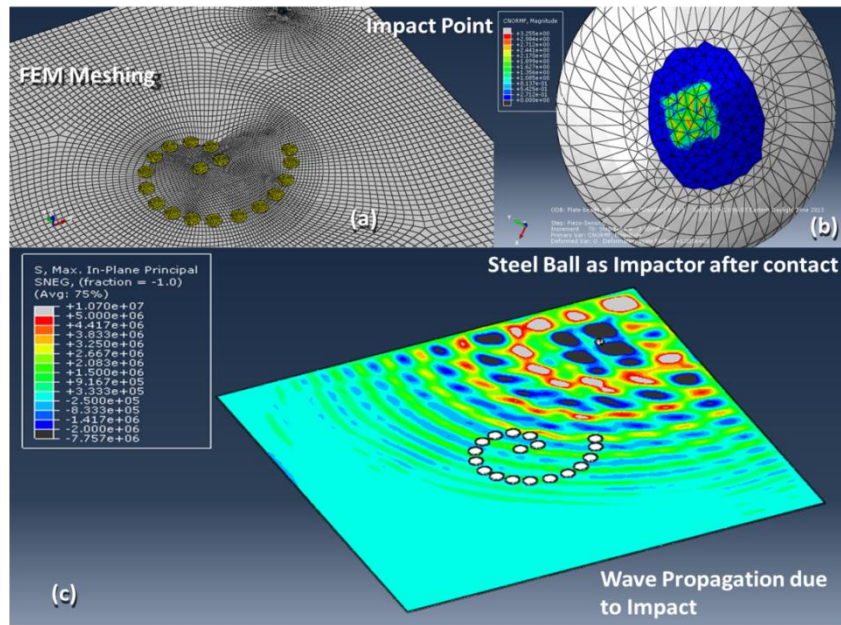
Figure 6.5 (a) Aluminum plate with Theodorus spiral sensor in FEM model fine meshed (b) the displacement of the steel ball after impact near the contact area (c) wave created in the plate after impact

In order to support experimental results, a CFFEM of the PMOI experiment was conducted. To limit the computation time, a 12 inch x 12 inch aluminum plate was modeled in ABAQUS, with in situ TSSC embedded. Impact of the steel ball shown in Figure 6.1 (b) at the location A (refer to section 6.1) is simulated with a drop height of 18.5 inch from the plate, similar to experimental conditions. Figure 6.5 shows the CFFEM meshing of the structure, while the generated guided waves acquired by the first three sensors with respect to the origin of the TSSC are displayed in Figure 6.6. TOA determined by the first significant amplitude did not cause any ambiguity. Similar operation described in the two previous sections was used to obtain PMOI. The

estimation of minimum error points was very close to experimental estimations, as will

be seen in the results section discussed next.
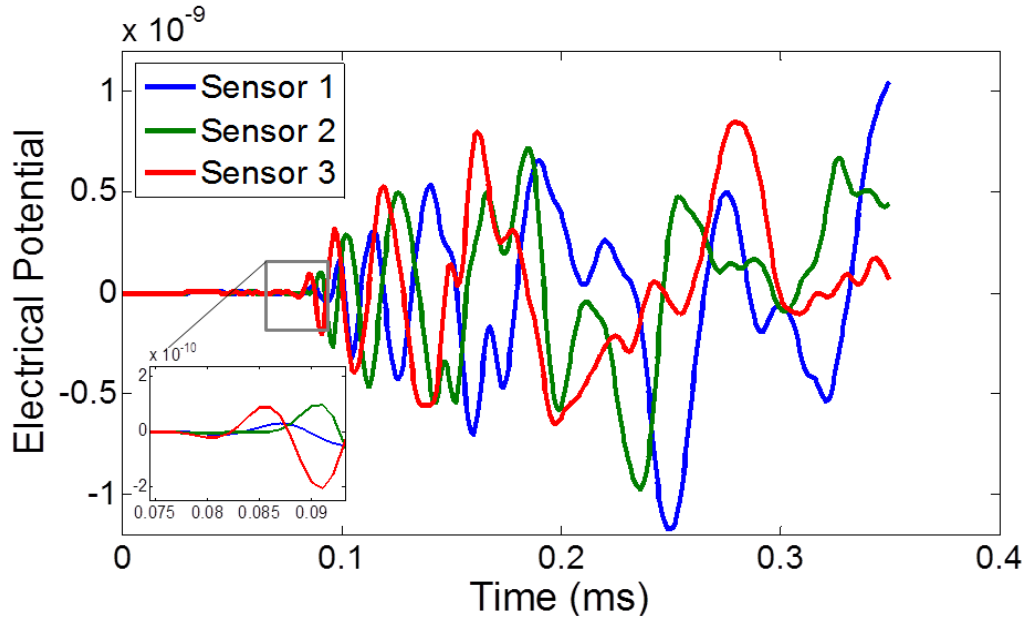
Figure 6.6 ABAQUS simulated sensor signals obtained from sensor 1, 2 and 3 in the TS
sensor configuration after impact. Clearly, the difference in TOA is observable

6.6 PMOI RESULTS AND DISCUSSIONS

A typical objective function using the equation (6.7) (for the 1st set of sensors,

combination 1, i.e. sensor number 1, 2 and 3) is plotted in Figure 6.7 (a). Corresponding

impact location is shown in Figure 6.7 (b) obtained from experiment and simulation.

The minimum value of the error function can be obtained by meshing the plate in

MATLAB. The coordinate of the minimum value of the error is recorded as probable

impact points. Next, the statistical analysis was performed as described in sections 6.3

and 6.4. All figures presented here are for the 12 inch x 12 inch middle portion of the

plate considered for further analysis, with origin set at one of its four top corners. Hence, sensor 1 is at the (6, 6) inch coordinate with respect to the origin.
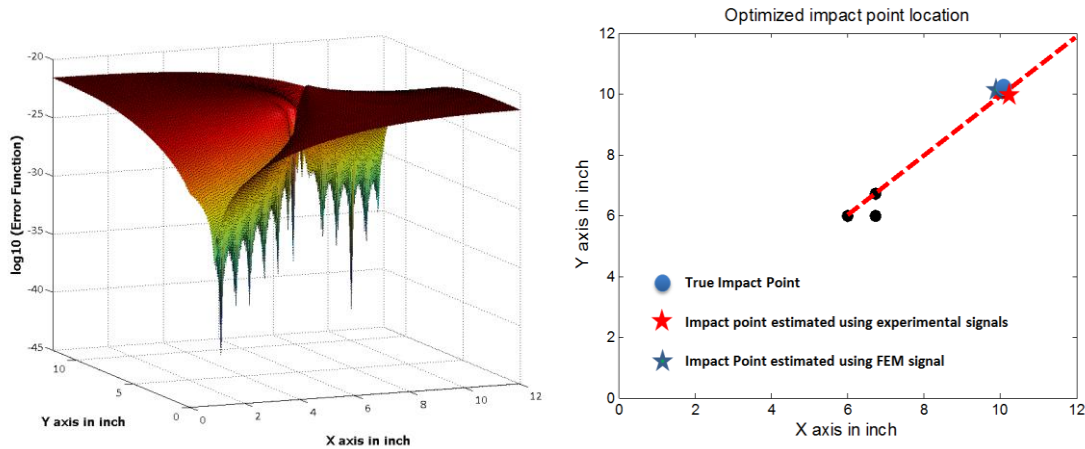
Figure 6.7 (a) Objective function or error function variation for three sensor set plotted in log scale (b) Impact point identification using 3 sensors

The proposed statistical analysis in equation (6.8) is performed on the data obtained from the error minimization step. In Figure 6.8, the PMOIs are presented for the impact on the plate with steel ball and golf ball accordingly, w.r.t. the impact locations, A and B. The figures in columns are presented to characterize the impact type and the figures in the rows are presented to classify the impact location. The 3D surface plots of the PMOIs are shown in Figure 6.9. The projections of the 3D plots on x-y plane are elliptic in geometry. Each ellipse represents equiprobability lines. Hence, the region of the plate within an ellipse prescribes were the impact point can be found with a certain confidence level. The center most ellipse is the most probable region of the impact event. The equiprobability lines can be seen in Figure 6.8. It can be observed that the true impact point for all cases falls within the 90% probability lines. From Figures 6.8 and

6.9, it is apparent that the major and minor axes of the ellipses representing equal probability lines are impact type dependent and direction of incoming wave dependent (i.e. direction w.r.t. the origin of the TSSC). The latter effect is due to the orientation of TSSC w.r.t. the incoming wave. Hence, using a single plot, many comments can be made about the most probable impact location, the direction of impact, and the impact type. Correlating sensor signals with the PMOIs, it can be deduced that high frequency waves excited by small and hard objects with small contact area cause a narrower distribution. On the other hand, low frequency waves excited by large and soft objects with large contact area cause a wider distribution. A calibration curve can be obtained from the CFFEM model in conjunction with experiments to derive PMOI that characterize impact types. As this master's thesis work aims at addressing the basic application of TSSC, extensive calibration step is omitted.

In Figure 6.8 the centermost ellipse is the most probable region of the true impact point, whereas the outermost ellipse represent least probable region of the true impact point. In Figure 6.9 the fitted probability density function can be seen with the z axis representing $f(x, y)$. Due to the inaccuracy of the measurement of the time-of-arrival, the estimated impact point location will vary and have a normal distribution. The probability density was significantly higher near the actual impact point location (e.g. estimated coordinate of the impact point due to a steel ball at point (2, 10) is at (2.091, 10.59), however, it is not necessary to obtain such impact point location because the proposed study is aimed to provide most probable region of impact after the impact event has occurred based on desired threshold probability, e.g. 98%. In anisotropic plate the velocity profile is extremely important to investigate beforehand when using triangulation

techniques. However, using the proposed technique a unique direction of impact can be predicted without having a velocity profile, if the TSSC largest dimension is much smaller than the impact distance from the TSSC. Also, the proposed technique is useful for obtaining the location of impacts where sensors cannot be widely or extensively distributed but clustered.
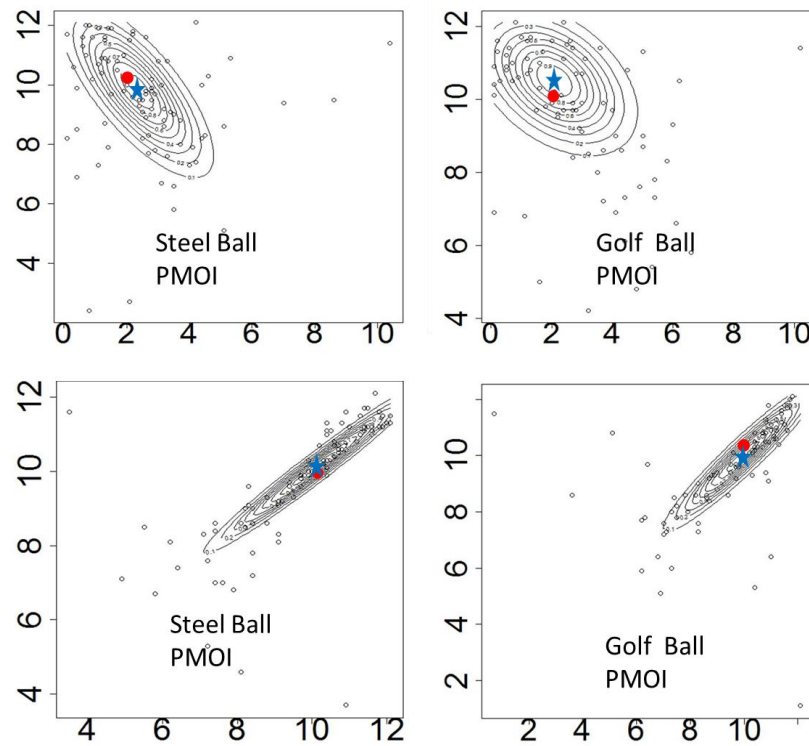
Figure 6.8 Contour Projection of the PMOI map calculated for every 10% change in probability. Red circle signifies the actual impact point and blue star signifies the estimated impact point, small black circles are the minimum error point from all the combination from TS sensors. Estimates are expected to be different than actual impact point because of inherent noise of the data but they are reasonably close. Although the estimated impact point is marked, the objective is to obtain a high POI region on the plate. The extents of major and minor axes of the ellipse obtained from equal probability lines are the measure of type of impact. Such parameters could be utilized for calibration of impact energy and thus could lead to classification of the impactors which inherently classify a steel ball and a golf ball in this sample study.

Figure 6.9 3D density plot of computed PMOI

CLOSING REMARKS

The concept of TSSC for the classification of low velocity, low energy impact events on plate was introduced and validated with CFFESs and experiments. The new approach proposes a chiral orientation of the passive sensors found in TS in conjunction with various models. The strategic orientation of the passive sensors were useful for directional, frequency and imapactor material sensitivity, and it minimized the need for prior knowledge of the velocity profile of the structu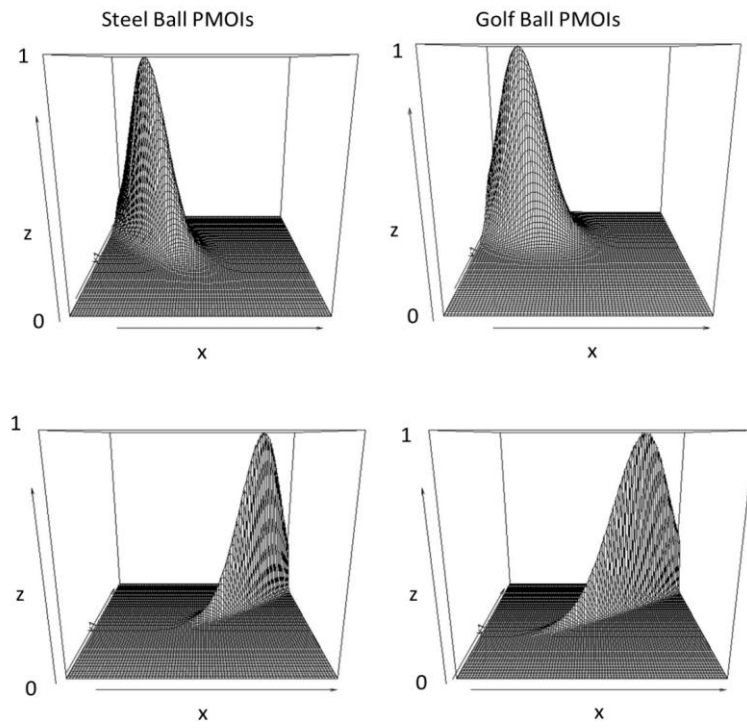re when determining the impact point based on a PMOI. As this approach is computationally inexpensive and applicable to real-time information in health monitoring systems, the algorithm can be specifically useful for the critical components of the structures where an extensive distribution of passive sensors may not be feasible or a clustered layout is preferred. We showed how TS geometry enhances frequency sensitivity, necessary for classifying the impactor elastic modulus, hence the impactor material and consequently, determining the force history. We found that the mutually distinct vertices inherent in the TS geometry boosted the efficacy of the models to distinguish impactor materials (e.g. stainless steel impactor from a marble impactor) and probabilistically determine the impact point.

For the revelation of these facts, multiple CFFESs and experiments were conducted. The first round of simulation and experiment was for evaluating the efficacy of TSSC in classifying the impactor material. In order to justify the CFFEM approach, the fundamental information obtained from the model was compared to empirical results. It

75

was found that the force history and the piezoelectric electrical potentials in both time and frequency domain were in agreement with experimental results. Consequently, preliminary DFB analysis was performed on sensor cluster data-sets obtained from the CFFEM, for the different impactor materials considered in this work. From this, we efficiently confirmed the enhanced wave mode sensitivity of TSSC over CSC and SSC, which simultaneously led to the classification of the impactor materials. From the preliminary test it was found that the DFB-FFT-TSSC was the most effective combination in classifying the impactor materials among its counterparts (i.e. DFB-FFT-CSC, DFB-FFT-SSC, DFB-STFT-TSSC, etc.). All data analysis focused on the P-wave packet, since the relationship of the impact event with the excited waves was subtle, discrepant and only properly correlated using this portion of the wave. A second round of experiment was conducted to validate the TSSC-DFB-FFT technique alongside LI technique. As a result the DFB-FFT-TSSC and LI techniques were established as conclusive physics-based methods for classifying the elastic modulus of impactors.

With the classified impactor materials, CZ theory was modified to obtain accurate impact force history solutions as a function of the impactor material property, algorithmically. This was achieved by implementing two empirically determined modification parameters controlled by the FETs. TSSC provided mutually exclusive data sets that enabled LI and DFB to have robust sensitivity to impactor elastic modulus. This was useful for identifying the soft impactors in order for the paramount and automated correction of corresponding force history solutions.

Lastly, the PMOI alternative approach was tested. For this a second round of CFFES and third round of experiment was conducted. Two different impacting objects –

76

a steel ball and a golf ball were tested. It was shown that a map of probable impact area, namely the PMOI, can be predicted without considering the velocity profile. A minimized error function and probability density function was applied to TSSC AUSs to determine this. It was also found that high frequency waves excited by small, hard objects with small contact area caused a narrower PMOI distribution. On the other hand, low frequency waves excited by large, soft objects with large contact area caused a wider PMOI distribution. Also the PMOI distribution was influenced by the direction of incoming wave w.r.t. the in situ TSSC.

RECOMMENDATIONS OF FUTURE RESEARCH

Studies on the classification of low velocity impact using the approach discussed in this thesis work can clearly be further researched and developed, as there is a lot more work to be done. Here is a list of recommended future works to explore.

1. Further work can be done using an anisotropic plate embedded with the TS sensor orientation to test the velocity independence of TSSC in the determination of impact point.

2. Future experiments and simulations can be conducted in order to classify more impact parameters such as impact contact area, impact velocity, etc. These studies will also seek to vary impactor mechanical as well as geometric properties over broader values with slight perturbation. The influence of the distance and direction of the impact event on the TSSC AUSs can be studied. More feature extraction techniques can be developed to model relationships. From such studies, a knowledge based ANN can be developed and the probable

force history of the impact event and consequent degree of damage can be predicted.

3. A system identification approach can be investigated to compare with the unconventional approach proposed in this work. To do this, the impulse response determined from a system identification approach for various impactor materials can be empirically validated and compared to the force histories obtained from the modified CZ theatrical approach.

REFERENCES

1.   Sohn H., Farrar C.R., Fugate M.L. and Czarnecki J.J. (2001). Structural Health Monitoring of Welded Connections. *The First International Conference on Steel & Composite Structures, Pusan, Korea.*

2.   Deraemaeker A. and Worden K. (2010). New Trends in Vibration Based Structural Health Monitoring. *CISM Courses and Lectures 520 SpringerWeinNewYork.* 1-6, 55-247.

3.   Mountain D.S. and Webber J.M.B. (1979). Stress Pattern Analysis by Thermal Emission (SPATE). *Proc. SPIE 0164, 4th European Electro-Optics Conf.* 189-193.

4.   Santulli C. (2000). Impact Damage Evaluation in Woven Composites using Acoustic and Thermoelastic Techniques. *PhD Dissertation, Department of Engineering Materials Science and Engineering, University of Liverpool, Liverpool, Merseyside L69 3BX, United Kingdom.* 73-79

5.   Gyekenyesi A.L. and Baaklini G.Y. (1999). Thermoelastic stress analysis: the mean stress effect in metallic alloys. *Proc. SPIE 3585, Nondestructive Evaluation of Aging Materials and Composites,* 3. 142-145.

6.   Tan K. (1995). Comparison of Lamb Waves and Pulse Echo in Detection of Near-Surface Defects in Laminate Plate. *NDT &E Int .* 28 215-23.

7.   Ghosh T., Kundu T. and Karpur P. 1998. Efficient Use of Lamb Modes for Detecting Defects in Large Plates. *Ultrasonics,* 36. 791-801.

8.   Tua P.S., Quek S. and Wang Q. 2004. Detection of Cracks in Plates using Piezo-actuated Lamb Waves. *Smart Mater. Struct,* 13. 643-60.

9.   Giurgiutiu V. (2008). Structural Health Monitoring with Piezo Wafer Active Sensors. *Elsevier.* 1-3, 503-587, 621-656.

10.   Oldewurtel F. and Mahonen P. (2006). Neural Wireless Sensor Networks. *RWTH Aechen University, Department of Wireless Networks In proceeding of: Systems and Networks Communications.* 3-5

11.   Rojas R. (1996). Neural Networks: A Systematic Introduction. *Springer, Berlin.*

12.   Rogers C.A. (1993). Intelligent Material Systems - The Dawn of a New Material Age. Journal of Intelligent Material Systems and Structures 4. 4-12

13.   Patnalk A., Anagnostou D.E., Mishra R.K., Christodoulou C.G. and Lyke J.C. (2004). Applications of Neural Networks in Wireless Communication. *IEEE Antennas and Propagation Magazine 46.* 130-135.

14.   Bayoumi A., Goodman N., Shah R. , Roebuck T., Jarvie A., Eisner L., Grant L. and Keller J. (2008). Conditioned-Based Maintenance at USC - Part III: Aircraft Components Mapping and Testing for CBM. *American Helicopter Society International, Inc.* 2-11

15.   Hassan M.A., Shin Y., Bayoumi A., Tarbutton J., Les Eisner M.G. and Higman J. (2013). Nonlinear Vibration-Interaction Metric for Health. *American Helicopter Society International, Inc.* 1-7.

16.   Molina G. (1994). On the Characterization of Impact Properties of Engineering Materials. An Acousto-Ultrasonics Patter Recognition Approach. A thesis work sumbmitted to the Faculty of Graduate Studies and Reserch, Department of Mechanical Engineering University of Ottawa.

17.   Yu L. and Giurgiutiu V. (2009). Multi-mode Damage Detection Methods with Piezoelectric Wafer Active Sensors. *Journal of Intelligent Material Systems and Structures* 20. 1336-1339

18.   Hayes B.S. and Gammnon L.M. (2010). Optical Microscopy of Fiber-Reinforced Composites. *ASM International.* 193-207.

19.   Goldstein J., Newbury D., Joy D., Lyman C., Patrick E., Lifshin E., Sawyer L. and Mickael J. (2003). Scanning Electron Microscopy and X-ray Microanalysis. *New York: Kluwer Academic/Plenum Publishers*. 21-29.

20.   Helm J.D., McNeill S.R. and Sutton M.A. (1996). Improved Three-dimensional Digital Image Correlation for Surface Displacement Measurement. *Society of Photo-Optical Instrumentation Engineers,* 35, 7. 1911-1919.

21.   Liu Z. S., Lee H. P. and Lu C. (2003). Structural Intensity Study of Plates under Low-Velocity Impact. *Int. Journal of Impact Engineering,* 31, 8. 957–975.

22.   Yang J.C.S. and Chun D.S. (1969). Application of the Hertz Contact Law to Problems of Impact in Plates. *United States Naval Ordnance Laboratory, White Oak, Maryland. NOLTR.* 69-152.

23.   Sun C.T. and Yang S.H. (1980). Contact Law and Impact Response of Laminated Composite. *NASA*. CR-159884.

24.   Suemasu H., Kerth S. and Maier M. (1994). Indentation of Spherical Head Indentors on Transversely Isotropic Composite Plates. *Journal of Composite Materials.* 28. 1723-1739.

25.   Liu Z. and Swaddiwudhipong S. (1997). Response of Plate and Shell Structures due to Low Velocity Impact. *Journal of Engineering Mechanics*. 1230-1237.

26.   Olsson R. (2002). Engineering Method for Prediction of Impact Response and Damage in Sandwich Panels. *Journal of Sandwich Structures and Materials* 4, 1 83-95.

27.   Zheng D. and Binienda W.K. (2009). Semianalytical Solution of Wave-Controlled Impact on Composite Laminates. *Journal of Aerospace Engineering,* 22, 3. 318-323.

28.   Zener C. (1941). The Intrinsic Inelasticity of Large Plates. *Physical Review,* 59. 669-673.

29.   Olsson R. (2002). Mass Criterion for Wave Controlled Impact Response of Composite Plates. *Composites,* 31, 8. 879-887.

30.   Lee H.P., Lu C., Liu Z.S., and Xu X.D. (2003). The Structural Intensity analysis of plates under dynamic loading. *Proceedings of the 16th Nordic Seminar on Computational Mechanics, Trondheim, Norway.* 145-148.

31.   Xu X.D., Lee H.P., Wang Y.Y., Lu. C. (2004). The Energy Flow Analysis in Stiffened Plates of Marine Structures. *Thin-Walled Structures,* 42. 979–994.

32.   Hurlebaus S., Niethammer M., Jacobs L.J. and Valle C. (2001). Automated Methodology to Locate Notches with Lamb Waves. *Acoust. Res. Lett. Online* 2. 97-102.

33.   Banz R., Niethammer M., Hurlebaus S. and Jacobs L.J. (2003). Localization of Notches with Lamb Waves. *Journal of Acoustic Society of America,* 114. 677-85.

34.   Ye L., Lin Y. and Zhongqing S. (2006). Crack Identification in Aluminum Plates Using Lamb waves Signals of a PZT Sensor Network. *Smart Materials and Structures,* 15.

35.   Raghavan A. and Cesnik C. (2007). Guided Wave Signal Processing using Chirplet Matching Pursuits and Mode Correlation for Structural Health Monitoring. Smart Materials and Structures, 16.

36.   Jata K.V., Kundu T, Parthasarathy T. An Introduction to Failure Mechanisms and Ultrasonic Inspection. *Advanced Ultrasonic Methods for Material and Structural Inspection*. Chap 1. 1-42.

37.   Giurgiutiu V. (2003). Lamb Wave Generation with Piezoelectric Wafer Active Sensors for Structural Health Monitoring. Proc *SPIE* 5056. 111-122.

38.   Marchi L.D., Marzani A., Speciale N. and Viola E. (2001). "A Passive Monitoring Technique based on Dispersion Compensation to Locate Impacts in Plate-like Structures," *Smart Mater. Struct* ,20.

39.   Mal A.K., Shih F., and Banerjee S. (2003). Acoustic Emission Waveforms in Composite Laminates under Low Velocity Impact. *Proc SPIE* 5057. 1-12.

40.   Mal A.K., Ricci F., Gibson S. and Banerjee S. (2003). Damage Detection in Structures from Vibration and Wave Propagation Data. *Proc SPIE* 5047, 1-12.

41.   Staszewaski WJ, Boller C, Tomlinson G.R. (2004). Health Monitoring and Aerospace Structures. *New York, Wiley.*

42.   Matt H. and Lanza di Scalea F. (2009). Macro Fiber Composite Piezoelectric Rosettes for Acoustic Source Location in Complex Structures. *Proc SPIE* 6529.

43.   Salamone S., Bartoli I., Di Leo P., Lanza di Scalea F., Ajovalasit A., D'Acquisto L., Rhymer J. and Kim H. (2010). High Velocity Impact Location on Aircraft Panels using Macro Fiber Composite Piezoelectric Rosettes. *Journal of Intelligent materials systems and structures* 21. 887-96.

44.   Salas K.I., Cesnik C.E.S. (2009). Guided Wave Excitation by a CLoVER Transducer for Structural Health Monitoring: Theory and Experiments. *Smart Mater. Struct.* 18.

45.   Park J., Ha S. and Chang F.K. (2009). Monitoring Impact Events using a System Identification Method. *AIAA Journal* 47. 2011-21.

46.   Staszewski W.J., Worden K., Wardle R. and Tomlinson G.R. (2000). "Fail Safe Sensor Distributions for Impact Detection in Composite Materials," *J. Smart Mat. Struct* 9. 298-303.

47.   Coverley P.T., Staszewski W.J. (2003). Impact Damage Location in Composite Structures using Optimized Sensor Triangulation Technique. *J. Smart Mat. Struct.* 12, 795-803.

48.   Mueller I., Larrosa C., Roy S., Mittal A., Lonkar K. and Chang F. (2009). An Integrated Health Management and Prognostic Technology for Composite

Airframe Structures. *Annual Conference of the Prognostics and Health Management Society.*

49.   Kundu T., Das S. and Jata K.V. (2007). Point of Impact Prediction in Isotropic and Anisotropic Plates from the Acoustic Emission Data. *Journal of Acoust. Soc. Am.*122. 2057-66.

50.   Kundu T., Das S. and Jata K.V. (2009). Detection of the Point of Impact on a Stiffened Plate by the Acoustic Emission Technique. *Smart Mater. Struct.* 18.

51.   Hajzergarbashi T., Kundu T. and Bland S. (2011). An Improved Algorithm for Detecting Point of Impact in Anisotropic Inhomogeneous Plates. *Ultrasonics* 51. 317-24.

52.   Tracy M. and Chang F. (1998). Identifying Impacts in Composite Plates with Piezoelectric Strain Sensors, Part 1: Theory. *J. Intell. Maer. Sys. Struct.* 9. 929.

53.   Seydel R. and Chang F. (2001). Impact Identification of Stiffened Composite Panels: I. System Development. *Smart Mater. Struct.* 10. 354-69.

54.   Kosel T., Grabec I. and Muzic P. (2000). Location of Acoustic Emission Sources Generated by Air Flow. *Ultrasonics* 38. 824-26.

55.   Gaul L. (1998). Identification of the Impact Location on a Plate using Wavelets. *Mech Syst. Signal Process*. 12. 783-95.

56.   Gaul L., Hurlebaus S. and Jacobs L. (2001). Localization of a Synthetic Acoustic Emission Source on the Surface of a Fatigued Specimen. *Res. Nondestruct. Eval* 13. 105-17.

57.   Ciampa F. and Meo M. (2011). Acoustic Emission Source Localization and Velocity Determination of the Fundamental Mode A0 using Wavelet Analysis and a Newton-based Optimization Technique. *Smart Mater Struct* 20.

58.   Deutsch W.A.K., Cheng A. and Achenbach J.D. (1997). Self-Focusing of Rayleigh Waves and Lamb Waves with a Linear Phased Array. *Research in Nondestructive Evaluation 9*. 81-95.

59.   Krim H. and Viberg M. (1996). Two Decades of Array Signal Processing Research: The Prametric Approach. *IEEE Signal Processing Magazine*. 68-81.

60.   Rathod V.T. and Mahapatra D.R. (2011). Ultrasonic Lamb Wave based Monitoring of Corrosion Type of Damage in Plate using a Circular Array of Piezoelectric Transducers. *NDT & E International 44(7)*. 628-636.

61.   Zou N and Nehorai A. (2009). Circular Acoustic Vector-Sensor Array for Mode Beanforming. *IEEE Transactions on Signal Processing 57(8)*. 3041-3051.

62.   Song Y. and Rahardja S. (2010). Beamforming of Circular Microphone Array with Sound Absorbent Cylinder. *18th European Signal Processing Conference*. 1949-1932.

63.   Byungseok Y. (2011). Guided Lamb Wave Based 2-D Spiral Phased Array for Structural Health Monitoring of Thin Panel Structures. PhD Dissertation University of Maryland, College Park. 60-144.

64.   Ziatdinov R. and Miura K.T. (2012). On the Variety of Planar Spirals and Their Applications in Computer Aided Design. *European Researcher 27 (8)*. 1227-1232.

65.	Bobe S. and Schaefer G. (2008). Image Processing and Image Registration on Spiral Architecture with saLib. *I.J. of Simulation 7(3).* 37-43.

66.	Schwartz E. (1980). Computation Anatomy and Functional Architecture of Striate Cortes: A Spatial Mapping Approach to Perceptual Coding. *Vision Research 20.* 645-669.

67.	Wu Q., He X. and Hintz T. (2007). Image Rotation without Scaling on Spiral Architecture. *Proc. Int. Conference on Parallel Distributed Processing Techniques and Applications 1.* 399-405.

68.	Wu Q, He X and Hintz T. (2004). Virtual Spiral Architecture. *Proc. Int. Conference on Computer Graphics, Visualization and Computer Vision.* 512-520.

69.	Davis P.J. (1923). Spirals: From Theodorus to Chaos. *AK Peters, Ltd.*

70.	Victorov A. (1967). Rayleigh and Lamb Waves. *Plenum Press New York.*

71.	Pavlou D.G., Bancila R., Lucaci G., Belc F., Dan D., Pavlou M.G., Tirtea A., Gruin A. and Baera C. (2007). An Exact Solution of the Plate on Elastic Foundation under Impact Loading. *3rd WSWAS International Conference on Applied and Theoretical Mechanics, Spain.* 79-83.

72.	Carretero-Gonza´lez R., Khatri D., Porter M.A., Kevrekidis P.G., and Daraio C. (2009). Dissipative Solitary Waves in Granular Crystals. *Physical Review Letters 102.*

73.	Hilber H.M., Hughes T.J.R., Taylor R.L. (1977). Improved Numerical Dissipation for Time Integration Algorithms in Structural Dynamics. *Earthquake Engineering and Structural Dynamics 5.* 283-292.

74.	Simulia Abaqus (2011). Version 6.11 Documentation. *Dassault Systèmes Simulia.*

75.	Puttock M.J. and Thwaite E.G. (1969). Elastic Compression of Spheres and Cylinders at Point and Line Contact. *National Standards Laboratory Technical Paper 25.* 7,8.

76.	Daraio C., Nesterenko V., Herbold E. and Jin S. (2004). Strongly Nonlinear Waves in a Chain of Teflon Beads. *American Institute of Physics, AIP Conference Proceedings, 845.* 1507-1510.

77.	Hertz H.R. (1882). Ueber die Beruehrung elastischer Koerper (On Contact between Elastic Bodies). *Gesammelte Werke (Collected Works) 1. Leipzig, Germany, 1895.*

78.	Taarantola A. (2005). Inverse Problem Theory and Methods for Model Parameter Estimation. *Society for Industrial and Applied Mathematics.*

79.	Morchen F. (2003). Time series feature extraction for data mining using DWT and DFT. *Data Bionics, Philipps-University Marburg, Hans-Meerwein-Strasse, 35032 Marburg, Germany.*

80.	Anstey J.S., Peters D.K. and Dawson C. (2007). An improved feature extraction technique for high volume time series data. *Proceedings of the Fourth conference on IASTED International Conference: Signal Processing, Pattern Recognition, and Applications.* 74-81.

81.	Ljung L. and Glad T. (1994). Modeling of Dynamic Systems. *Upper Saddle River, NJ. Prentice Hall.*

82.	Orfanidis S.J. (1996). Optimum Signal Processing: An Introduction. 2nd Edition. *Englewood Cliffs, NJ: Prentice Hall.*

83.   Degroot M.H. and Schervish M.J. (2012). Probability and Statistics, 4th edition, Pearson
84.   Hahne F., Huber W., Ruschhaupt M. and Toedling J. (2012). "prada" R-package.